

# Searching for intergalactic star forming regions in Stephan's Quintet with SITELLE: II. Physical properties and metallicity

S. Duarte Puertas<sup>1</sup>, J. M. Vilchez<sup>1</sup>, J. Iglesias-Páramo<sup>1</sup>, L. Drissen<sup>2,3</sup>, C. Kehrig<sup>1</sup>, T. Martin<sup>2,3</sup>, E. Pérez-Montero<sup>1</sup>, and A. Arroyo-Polonio<sup>1</sup>

<sup>1</sup> Instituto de Astrofísica de Andalucía - CSIC, Glorieta de la Astronomía s.n., 18008 Granada, Spain  
e-mail: salvini@iaa.es

<sup>2</sup> Département de physique, de génie physique et d'optique, Université Laval, Québec (QC), G1V 0A6, Canada

<sup>3</sup> Centre de recherche en astrophysique du Québec

Received September 23, 2020; accepted September 23, 2020

## ABSTRACT

Based on SITELLE spectroscopy data we studied the ionised gas emission for the 175 H $\alpha$  emission regions in the Stephan's Quintet (SQ) found in the companion paper [Duarte Puertas et al. \(2019\)](#). In this paper we perform a detailed analysis of the star formation rate (SFR), oxygen abundance and nitrogen-to-oxygen abundance ratio (N/O) of the SQ regions, intended to tackle on the provenance and evolution of this complex structure. According to the BPT diagram, we found 91 HII, 17 composite, and 7 AGN-like regions in SQ. Several regions are compatible with fast shocks models without precursor for solar metallicity and low density ( $n = 0.1 \text{ cm}^{-3}$ ), with velocities in the range of 175 – 300  $\text{km s}^{-1}$ . We derived the total SFR in SQ ( $\log(\text{SFR}/M_{\odot} \text{ yr}^{-1}) = 0.496$ ). Twenty-eight percent of the total SFR in SQ comes from starburst A (SQA), while 9% is in starburst B (SQB), and 45% comes from the regions with radial velocity lower than 6160  $\text{km s}^{-1}$ . For this reason, we assume that the material prior to the collision with the new intruder does not show a high SFR, and therefore SQ was apparently quench. When considering the integrated SFR for the whole SQ and the new intruder, we found that both zones have SFR consistent with those obtained in the SDSS star-forming galaxies. At least two chemically different gas components cohabit in SQ where, on average, the regions with high radial velocities ( $v > 6160 \text{ km s}^{-1}$ ) have lower values of oxygen abundance and N/O than those with low radial velocities ( $v \leq 6160 \text{ km s}^{-1}$ ). The values found for the line ratios considered in this study as well as in the oxygen abundance and N/O for the southern debris region and the northernmost tidal tail are compatible with regions belonging to the outer part of the galaxies. We highlight the presence of inner-outer variation for metallicity and some emission line ratios along the new intruder strands and the YTT South strand. Finally, the SQ H $\alpha$  regions are outside the galaxies because the interactions have dispersed the gas to the peripheral zones.

**Key words.** galaxies: general – galaxies: shock – galaxies: Stephan's Quintet – galaxies: NGC 7319 – galaxies: HCG 92 – galaxies: SITELLE

## 1. Introduction

The Stephan's Quintet (SQ) is a compact group of galaxies discovered by [Stephan \(1877\)](#). SQ is formed by two elliptical (NGC7317 and NGC7318A), three spiral (NGC7318B, NGC7319, NGC7320c), and one new dwarf galaxy described recently in [Duarte Puertas et al. \(2019\)](#), hereafter paper I). Also, in the field-of-view (FoV) of SQ we can see a foreground galaxy (NGC7320) with a discordant distance. In SQ we found diverse structures (e.g. tidal tails), but probably the most remarkable one is the large-scale shock region (LSSR, e.g. [Allen & Hartsuiker 1972](#); [Ohyama et al. 1998](#); [Iglesias-Páramo et al. 2012](#)) produced by the collision between NGC7318B and both NGC7319 and debris material produced from previous interactions. In paper I we found five velocity systems in SQ: i)  $v = [5600-5900] \text{ km s}^{-1}$ ; ii)  $v = [5900-6100] \text{ km s}^{-1}$ ; iii)  $v = [6100-6600] \text{ km s}^{-1}$ ; iv)  $v = [6600-6800] \text{ km s}^{-1}$ ; and v)  $v = [6800-7000] \text{ km s}^{-1}$  (see paper I for more details).

Previous works studied physical and chemical properties of star-forming objects in SQ (e.g. [Mendes de Oliveira et al. 2004](#); [Konstantopoulos et al. 2014](#)). The work by [Konstantopoulos et al. \(2014\)](#) studied the properties of 40 H $\alpha$  emitting regions in the LSSR, the new intruder (NI), and the southern debris region (SDR) and did not find shocked gas associated with the

HII regions or the intrusive galaxy. Massive star formation in regions of the shock zone appears substantially suppressed while the starburst A (SQA) region appears to be the most active star-forming region in the SQ ([Konstantopoulos et al. 2014](#)). The shocked gas presents two velocity components: low velocity ( $\leq 6160 \text{ km s}^{-1}$  and nearly solar metallicities<sup>1</sup>) and high velocity ( $> 6160 \text{ km s}^{-1}$  and low metallicity) ([Iglesias-Páramo et al. 2012](#); [Rodríguez-Baras et al. 2014](#)). The SDR presents typical star formation rate (SFR) values of nearby galaxies ([Konstantopoulos et al. 2014](#)) and its HII regions have subsolar metallicities, presenting a metallicity gradient along the spiral arm of NGC7318B ([Iglesias-Páramo et al. 2012](#)).

In this work we performed a detailed analysis of SQ based on the spectroscopic data from SITELLE ([Grandmont et al. 2012](#)), an imaging Fourier transform spectrometer (IFTS), attached to the Canada-France-Hawaii Telescope (CFHT). SITELLE has a large FoV ( $11' \times 11'$ ;  $0.32''$  per pixel, [Drissen et al. 2019](#)), and covers the optical range from 3500 Å to 7500 Å. It allows us to obtain a more complete view of the ionisation structure of the SQ and its physical and chemical properties. Previous spectroscopic studies are based on long-slit observations or Integral Field Units (IFU) with a smaller FoV which do not cover the whole area of

<sup>1</sup> Solar metallicity:  $12 + \log(\text{O}/\text{H}) = 8.69$  ([Asplund et al. 2009](#)).

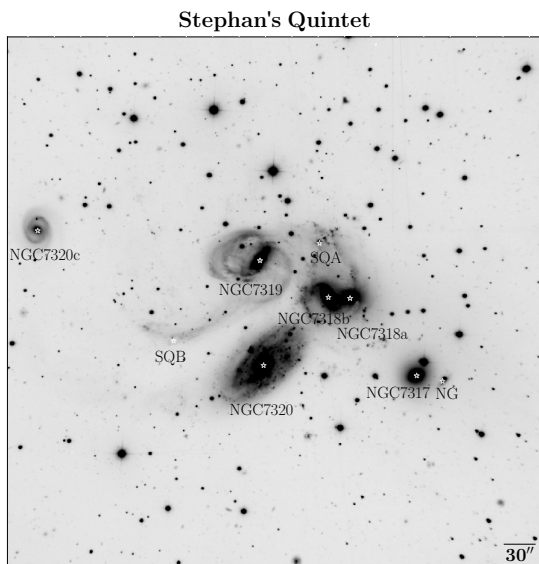


**Fig. 1.** SITELLE deep-grayscale image of SQ composed using SN1, SN2, and SN3 data cubes. North is top and East is left. The distance considered for SQ in this paper is  $d = 88.6$  Mpc (from the NASA/IPAC Extragalactic Database known as NED). At the distance of SQ,  $30''$  corresponds to  $\sim 13.04$  kpc.

the SQ (e.g. Iglesias-Páramo et al. 2012; Konstantopoulos et al. 2014). Thanks to the large FoV of SITELLE we can cover almost the entire SQ with a reasonable spectroscopic and spatial resolution.

In this work the determination of the gas metallicity, using oxygen abundance (O/H) as a proxy, allows us to distinguish between evolved metal-rich gas from the SQ galaxies and tidal tails, and identify unevolved metal-poor gas from the intergalactic medium (IGM). It is known that while representative dwarf galaxies present typical values of  $12+\log(\text{O}/\text{H})$  between 7.1 and 8.4 (van Zee & Haynes 2006; Croxall et al. 2009; Berg et al. 2012; Lee-Waddell et al. 2018), tidal dwarf galaxies present values higher than 8.4 (de Mello et al. 2012; Duc et al. 2014; Lelli et al. 2015). The combination of the results obtained in the three dimensional study from paper I with the SQ properties derived here (e.g. SFR, O/H, N/O, extinction, and diagnostic line ratios) leaves us in an excellent position to try to answer fundamental questions about the SQ, as for example: Is star formation inhibited for this group of galaxies? Where is located the star formation in SQ? Does the star formation occur outside the galaxies of SQ or not? Does the new intruder chemically enrich the environment? Is extinction associated with the highest star formation zones? Are we seeing different gas components cohabiting in SQ?

The structure of this paper is organised as follows: in Sect. 2 we detail our main results. Discussion and summary of our work are presented in Sect. 3. Throughout the paper, we assume a Friedman-Robertson-Walker cosmology with  $\Omega_{\Lambda 0} = 0.7$ ,  $\Omega_{m0} = 0.3$ , and  $H_0 = 70 \text{ km s}^{-1} \text{ Mpc}^{-1}$ .

## 2. Results

### 2.1. SITELLE spectroscopy. Line fluxes

Figure 1 shows a SITELLE deep-grayscale image of SQ field. We considered the sample of 175 SQ  $H\alpha$  emission regions

defined in paper I. For each  $H\alpha$  emission region we fitted the emission lines that we found in the SN1, SN2, and SN3 data cubes: e.g.  $[\text{O II}]\lambda 3727$ ,  $H\beta$ ,  $[\text{O III}]\lambda 4959, 5007$ ,  $H\alpha$ ,  $[\text{N II}]\lambda 6548, 6584$ , and  $[\text{S II}]\lambda 6717, 6731$ . The data analysis followed is described in details in paper I. It should be noted that the emission lines were fitted with sincgaussian functions (the convolution of a Gaussian with a sinc function) using the Python-based package ORCS (Martin et al. 2015). The fit output parameters are the radial velocity, broadening, intensity peak, total flux, and the corresponding uncertainties. All SQ  $H\alpha$  regions were defined according to the following criteria: the radial velocity of the region is within the radial velocity range of SQ (between  $\sim 5600$  and  $\sim 7000 \text{ km s}^{-1}$ ) and at least one additional emission line besides  $H\alpha$  was detected in the data cubes. From the sample of 175 SQ  $H\alpha$  regions, 127 (73%) present signal-to-noise ratio, SNR,  $\text{SNR}([\text{O II}]\lambda 3727) \geq 3$ , 169 (96%)  $\text{SNR}(H\beta) \geq 3$ , 131 (75%)  $\text{SNR}([\text{O III}]\lambda 5007) \geq 3$ , and 146 (83%)  $\text{SNR}([\text{N II}]\lambda 6584) \geq 3$ . We defined the SNR as the ratio of the flux to the statistical error flux, calculated with the pipeline ORCS (Martin et al. 2015).  $[\text{O III}]\lambda 5007$  and  $[\text{O II}]\lambda 3727$  are not detected in some regions of the North lobe, NGC7319 ‘arm’, and Shs. In Fig. 2 we show the emission line maps for  $[\text{O II}]\lambda 3727$ ,  $H\beta$ ,  $[\text{O III}]\lambda 5007$ ,  $H\alpha$ , and  $[\text{N II}]\lambda 6584$  for SQ when the SNR in each of them is greater than or equal to 3. For the regions with two velocity components, we consider the sum of the flux value of both components. As noted in paper I, we separated the SQ emission regions in two sub-samples: lower radial velocity sub-sample (LV) for those regions where the radial velocity is lower than or equal to  $6160 \text{ km s}^{-1}$ ; and the higher radial velocity sub-sample (HV) for all regions with radial velocity higher than  $6160 \text{ km s}^{-1}$ .

We corrected the emission line fluxes for reddening using the theoretical case B recombination (theoretical Balmer decrement,  $I_{H\alpha}/I_{H\beta} = 2.86$ ; electron temperature  $T = 10^4 \text{ K}$ , and low-density limit  $n_e \sim 10^2 \text{ cm}^{-3}$ ; Osterbrock 1989; Storey & Hummer 1995) together with the Cardelli et al. (1989) extinction curve with  $R_v = A_v/E(B - V) = 3.1$  (O’Donnell 1994; Schlegel et al. 1998), where  $A_v = 2.5 c(H\beta)$ . When the reddening coefficient,  $c(H\beta)$ , is negative we set it as zero. The Galactic extinction is very small in the direction of SQ,  $E(B - V) = 0.07$  according to NED<sup>2</sup>, and its contribution to  $A_v$  derived for each region is not relevant.

In Table C.1 we present emission line fluxes divided by  $H\beta$  and corrected for reddening for the SQ  $H\alpha$  emission regions. Only line fluxes with SNR greater than or equal to 3 are listed in Table C.1. In Col. 1 the region name is presented. Cols. 2, 3, 4, 5, 6, and 7 show the  $[\text{O II}]\lambda 3727$ ,  $[\text{O III}]\lambda 5007$ ,  $H\alpha$ ,  $[\text{N II}]\lambda 6584$ ,  $[\text{S II}]\lambda 6716$ , and  $[\text{S II}]\lambda 6731$  emission line fluxes, respectively. Col. 8 shows  $A_v$ , and Col. 9 tells us whether the velocity of the region belongs to the LV (0) or HV (1).

In Fig. 3 we show the 12 zones and 28 sub-zones defined in paper I for SQ as follows: i) young tidal tail (YTT) (e.g. Lisenfeld et al. 2002), so that North and South strands are respectively YTTN and YTTS, and NGC7320c is the old intruder (OI); ii) NGC7319 (NGC7319 nucleus, NGC7319 ‘arm’, North lobe); iii)  $H\alpha$  ‘bridge’; iv) high radial velocity strands, Hs (H1 and H2); v) SQA (e.g. Xu et al. 1999); vi) low radial velocity strands, Ls (L1, L2, L3, and L4); vii) shock strands, Shs (Sh1, Sh2, Sh3, and Sh4); viii) North and South of SQA (NSQA and SSQA, respectively); ix) tidal tail at North of NSQA (NW, e.g. Renaud et al. 2010); x) NI (e.g. Moles et al. 1997) strands, NIs (NI1, NI2, NI3, NI4, and NI5); xi) southern debris region (SDR,

<sup>2</sup> <http://ned.ipac.caltech.edu/>



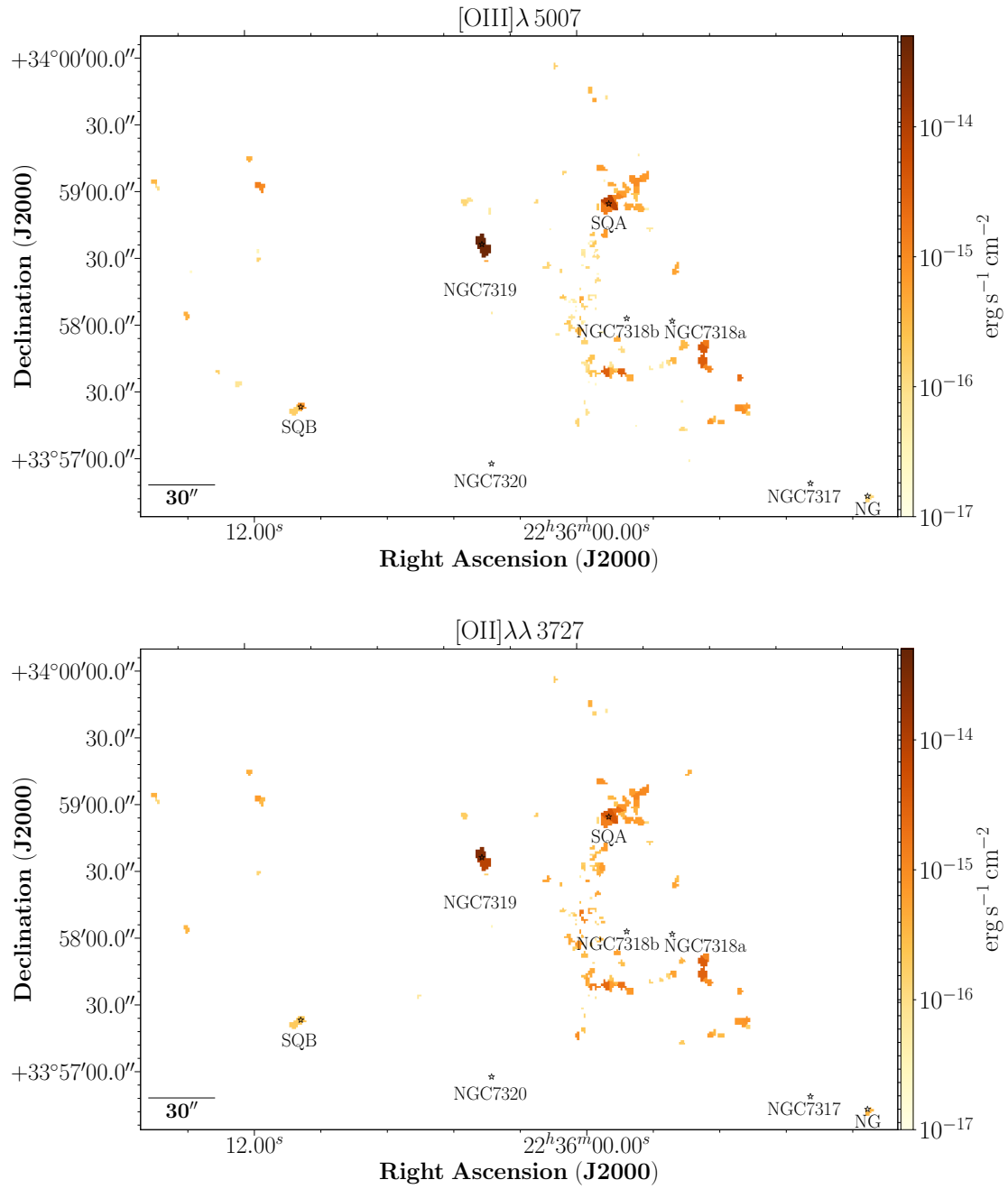
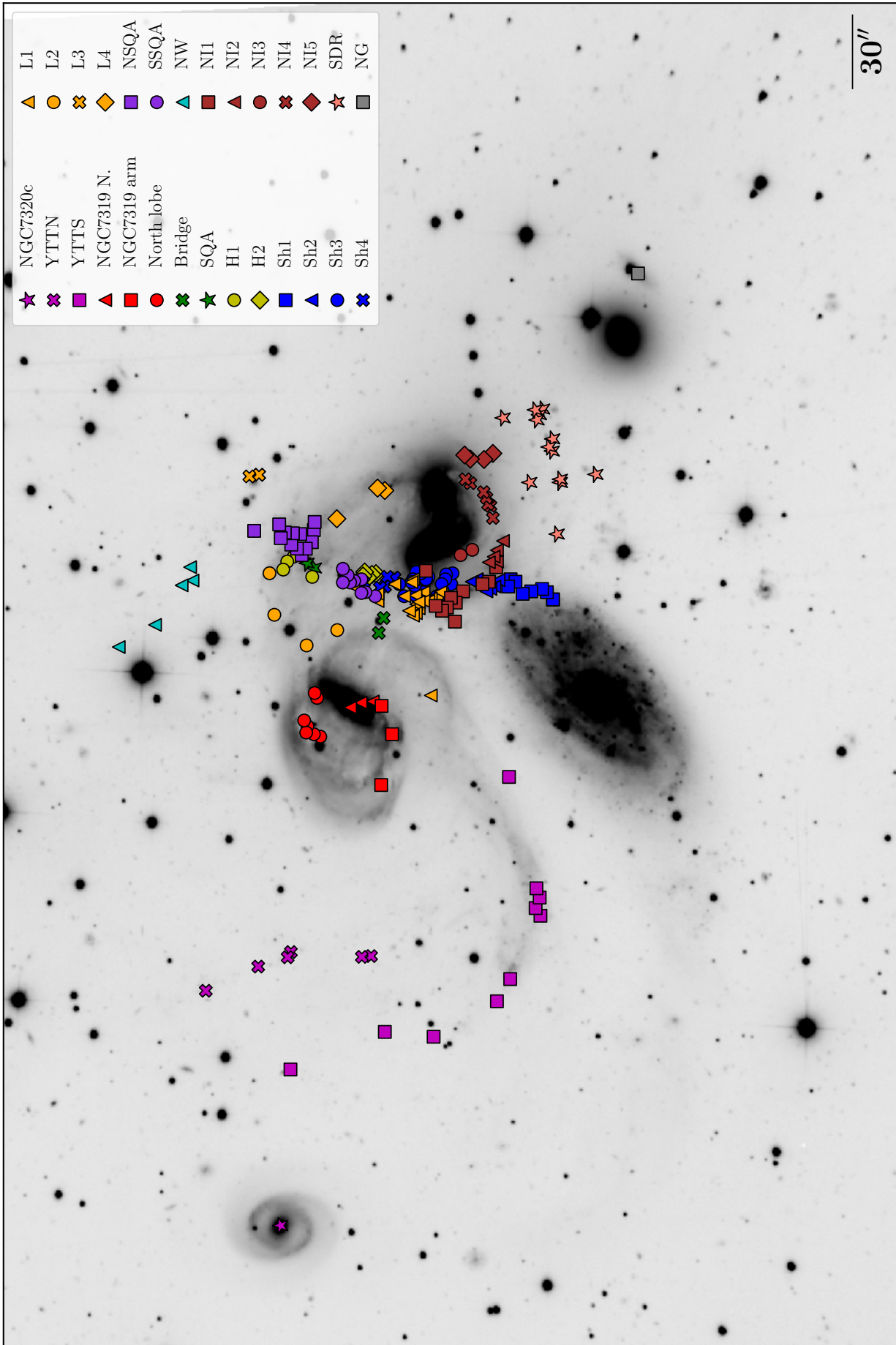


Fig. 2. (continued)

e.g. Fedotov et al. 2011); and xii) the new dwarf galaxy (NG). In Appendix A we detail all the zones defined here.



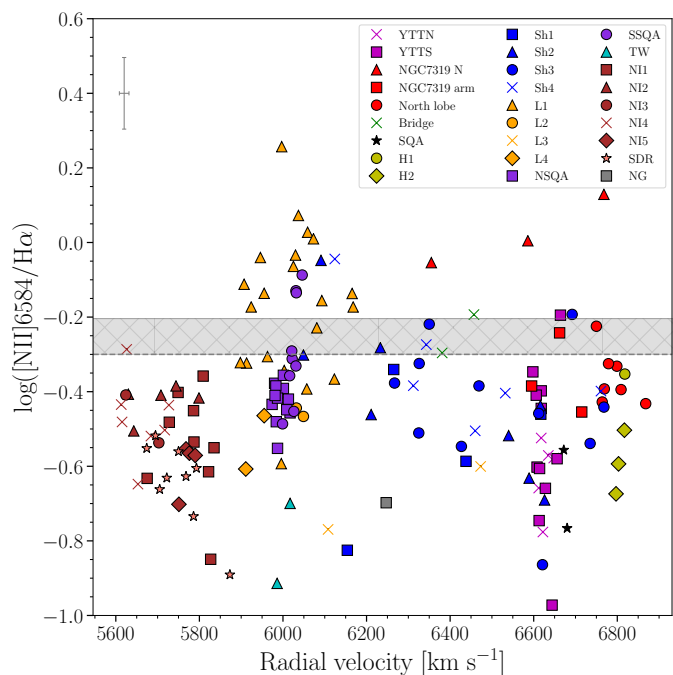
**Fig. 3.** Different systems of emission line objects defined here and indicated on SITELLE deep-grayscale image of SQ. Shown are the positions of YTTN and YTTS (magenta crosses and squares, respectively); NGC7319 nucleus, 'arm', and North lobe (red triangles, squares, and circles, respectively); bridge (green crosses); SQA (green stars); Hs (H1: yellow circles; H2: yellow diamonds); Shs (Sh1: blue squares; Sh2: blue triangles; Sh3: blue circles; Sh4: blue crosses); Ls (L1: orange triangles; L2: orange circles; L3: orange crosses; L4: orange diamonds); NSQA and SSQA (violet squares and circles); NW (cyan triangles); NIs (NI1: brown squares; NI2: brown triangles; NI3: brown circles; NI4: brown crosses; NI5: brown diamonds); SDR (salmon stars); and NG (grey squares).

## 2.2. Distribution of emission line ratios

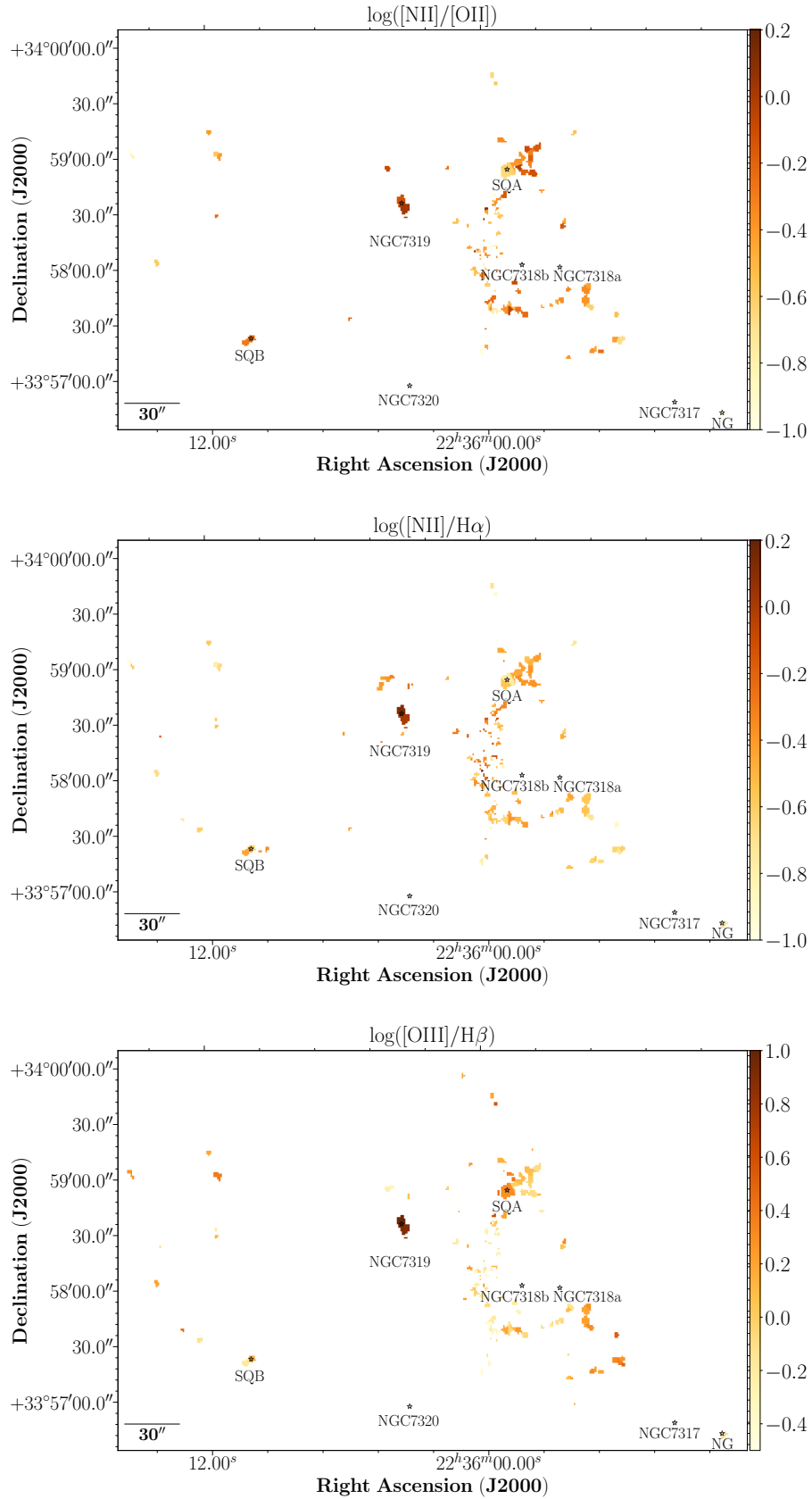
In this section we study the spatial distribution in the SQ of several emission-line ratios considered in the literature as proxies of oxygen abundance indicators (e.g.  $[\text{N II}]/\text{H}\alpha$ ,  $R_{23}$ ,  $\text{O3N2}$ ) and of the ionisation degree of the regions (e.g.  $[\text{O III}]/[\text{O II}]$ ). Some of them were not corrected for reddening given the proximity in wavelength of the emission lines involved (e.g.  $[\text{N II}]/\text{H}\alpha$  or  $[\text{O III}]/\text{H}\beta$ ). On the contrary,  $R_{23}$ ,  $[\text{O III}]/[\text{O II}]$ , and  $[\text{N II}]/[\text{O II}]$  need to be corrected for reddening according to Sect. 2.1. We calculated the values of  $R_{23} = \frac{[\text{O III}]\lambda 3727 + [\text{O III}]\lambda 4959,5007}{\text{H}\beta}$  (Pagel et al. 1979),  $[\text{O III}]/[\text{O II}] = \frac{[\text{O III}]\lambda 4959,5007}{[\text{O II}]\lambda 3727}$  (Díaz et al. 2000),  $\text{O3N2} = \frac{[\text{O III}]\lambda 5007/\text{H}\beta}{[\text{N II}]\lambda 6584/\text{H}\alpha}$  (Alloin et al. 1979) for the  $\text{H}\alpha$  regions.

Figure 4 shows the relation between  $\log([\text{N II}]/\text{H}\alpha)$  and radial velocity for all the regions in SQ. In the figure, the horizontal dashed grey line and the grey band correspond to the reference value at  $\log([\text{N II}]/\text{H}\alpha) = -0.3$  and the uncertainties for the  $\log([\text{N II}]/\text{H}\alpha)$  ratio, respectively. Regions with  $\log([\text{N II}]/\text{H}\alpha) \leq -0.2$  are assumed to be HII-like regions, while those with  $\log([\text{N II}]/\text{H}\alpha) > -0.2$  are related with shocked gas or AGNs (see Sect. 2.3). For the LV sub-sample, practically all the regions in NIs, SDR, NSQA, L2, L3, L4, and NW have values lower than  $-0.2$  for  $\log([\text{N II}]/\text{H}\alpha)$ . In contrast, L1 and SSQA show values higher than  $-0.2$  for  $\log([\text{N II}]/\text{H}\alpha)$ . In the HV sub-sample, most of the regions have values lower than  $-0.2$  for  $\log([\text{N II}]/\text{H}\alpha)$ , except the NGC7319 nucleus,  $\text{H}\alpha$  ‘bridge’, and several regions from Shs, North lobe, and the NGC7319 ‘arm’.

Figure 5 shows the line ratio maps in SQ considering the emission line maps from Fig. 2 (from top to bottom:  $\log([\text{N II}]/[\text{O II}])$ ,  $\log([\text{N II}]/\text{H}\alpha)$ ,  $\log([\text{O III}]/\text{H}\beta)$ ,  $\log(\text{O3N2})$ ,  $\log([\text{O III}]/[\text{O II}])$ , and  $\log(R_{23})$ ). The values for the line ratios for SDR and NW are compatible with those of regions detected in the outer discs of galaxies since they have low  $[\text{N II}]/\text{H}\alpha$  values, and high  $[\text{O III}]/\text{H}\beta$ ,  $\text{O3N2}$ , and  $[\text{O III}]/[\text{O II}]$  values (see Rodríguez-Baras et al. 2018, for more information about inner and outer HII regions over the discs of spiral galaxies). The values derived for SQA are compatible with those of the outer regions of the galaxies, and could also match typical values for a tidal dwarf galaxy. YYTS has an inner-outer gradient presenting lower  $[\text{N II}]/\text{H}\alpha$  and higher values for  $[\text{O III}]/\text{H}\beta$  and  $\text{O3N2}$  in the West than in the East. The LSSR presents high  $[\text{N II}]/[\text{O II}]$  values, and low  $[\text{O III}]/\text{H}\beta$ ,  $\text{O3N2}$ , and  $[\text{O III}]/[\text{O II}]$  values. With these results we can see how the regions from the LSSR have values of emission-line ratios completely different from the rest of the SQ zones studied.



**Fig. 4.**  $\log([\text{N II}]/\text{H}\alpha)$  versus radial velocity diagram. All the points in the figure have the same colours and markers as Fig. 3. The horizontal dashed grey line and the grey band correspond to the reference value at  $\log([\text{N II}]/\text{H}\alpha) = -0.3$  and the uncertainties for the  $\log([\text{N II}]/\text{H}\alpha)$  ratio, respectively. The upper left cross indicates the typical error of both parameters.



**Fig. 5.** Line ratios maps. From top to bottom:  $[\text{NII}]\lambda 6584/[\text{OII}]\lambda 3727$ ,  $[\text{NII}]\lambda 6584/\text{H}\alpha$ ,  $[\text{OIII}]\lambda 5007/\text{H}\beta$ , O3N2,  $[\text{OIII}]\lambda 5007/[\text{OII}]\lambda 3727$ ,  $R_{23}$ .

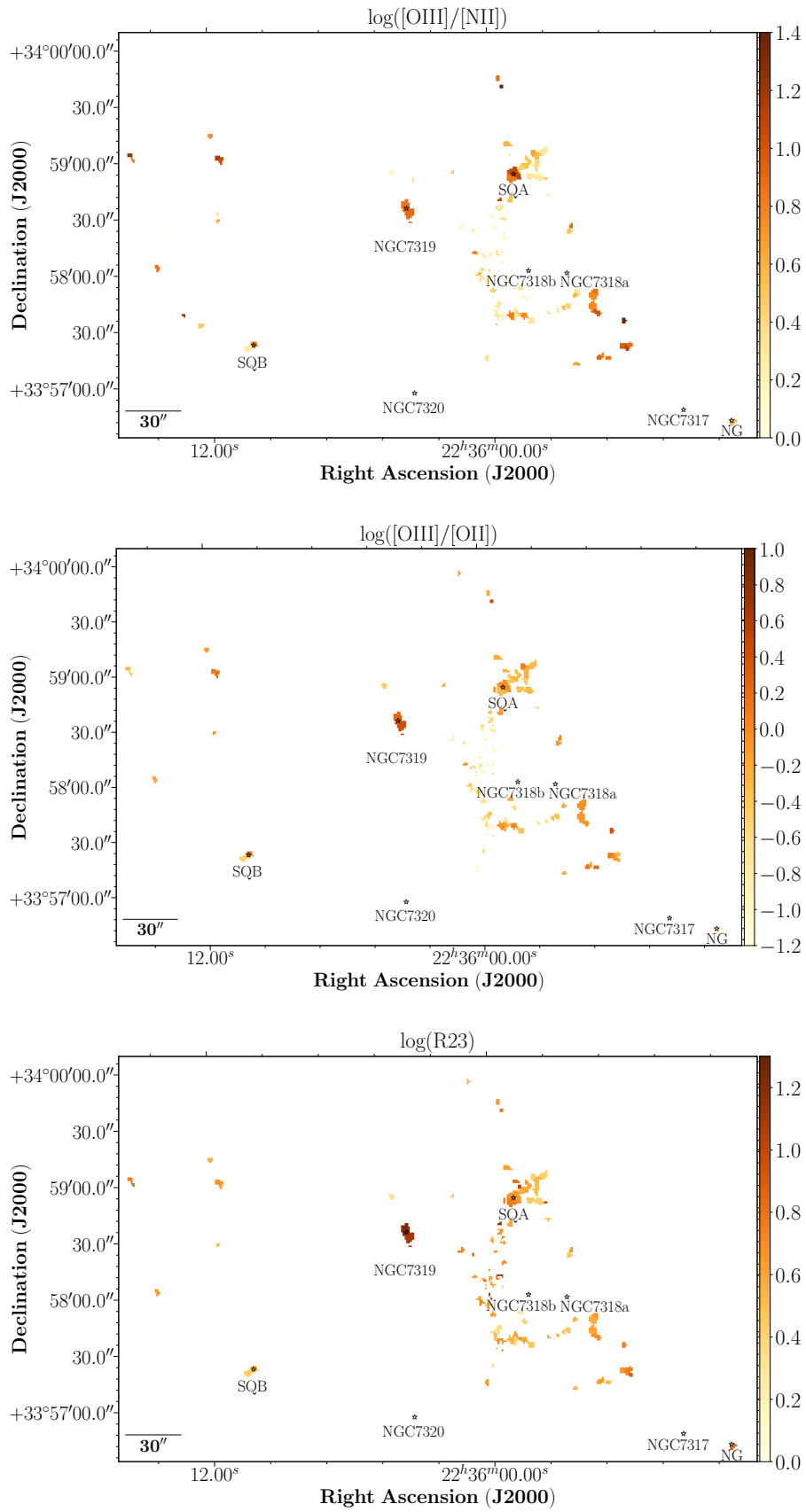
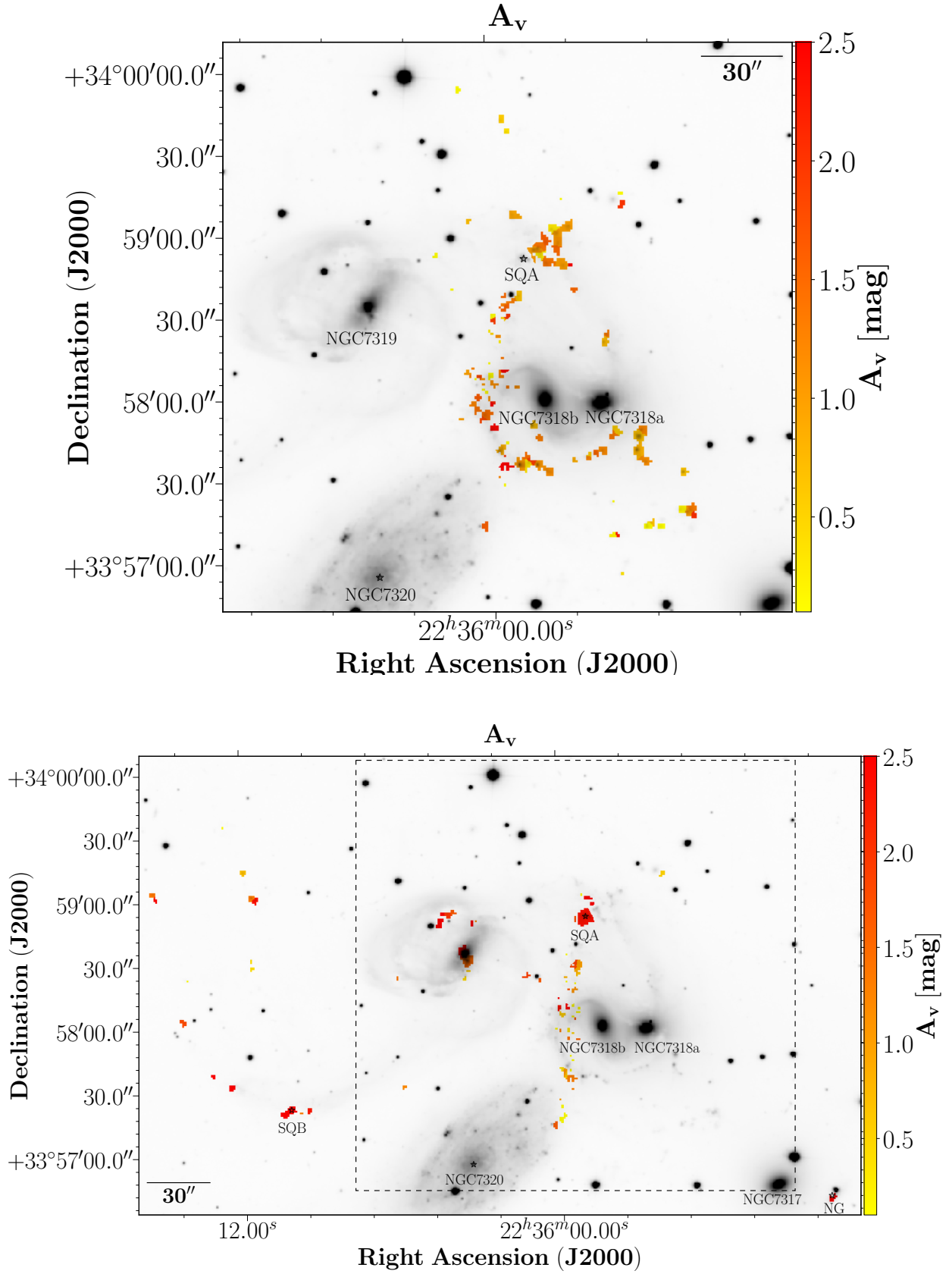


Fig. 5. (continued)



**Fig. 6.** SQ spatial map colour coded according to their  $A_v$  extinction for the LV sub-sample (upper panel) and the HV sub-sample (lower panel).

### 2.3. Maps of extinction and excitation

In Fig. 6 we show the extinction map in magnitudes in the V band,  $A_v$ , for the emission regions found in SQ. We separate the maps in LV (upper left panel) and HV (upper right panel) sub-samples according to the definition given in Sect. 2.1. The extinction  $A_v$  derived in this work goes from 0 to 4 mag. The median is  $A_v = 1.1$  mag, in agreement with the value obtained in Rodríguez-Baras et al. (2018) for a sample of star-forming regions over the discs of spiral galaxies. On average, the regions found in LV show lower values of  $A_v$  ( $\sim 1$  mag) than those located in HV ( $\sim 1.3$  mag), in line with previous works (e.g. Konstantopoulos et al. 2014). In LV extinction map we can see several interesting distributions. SDR presents  $A_v$  values  $\sim 0.5$  mag. Moreover, in North and South of the strong HII region SQA (NSQA and SSQA, respectively) a mixture of  $A_v$  values are found. Generally, SSQA has higher  $A_v$  values than NSQA (SSQA:  $\sim 1.3$ ; NSQA:  $\sim 1$ ). Region 66 has a  $A_v \sim 2.9$  (from L1), being the region with the greatest value in the LV map. On the other hand, SQA has an extinction value  $A_v \sim 2.3$  mag. In the AGN North lobe we can see  $A_v > 1.2$  mag, where the greatest value is seen in the region 20 ( $A_v \sim 4.2$  mag, see Table C.1). NG has also high extinction (with average  $A_v \sim 3.5$  mag). YTTs presents higher extinction values, on average, than in the North regions, where the extinction values are lower than 2.5 mag. Conversely, in the LSSR zone, a mixture of extinction values are found (with a median value of  $A_v \sim 1$  mag). It is important to note that at the centre of the LSSR zone, several regions with  $A_v > 2$  mag (e.g. region 83 and 60) are present in both LV and HV maps.

In this work, we are interested in the study of the properties of the SQ HII regions. In order to produce a classification of the emitting regions, we study the BPT diagnostic diagram (Baldwin et al. 1981; Kewley et al. 2001; Kauffmann et al. 2003). In Fig. 7 we show the BPT diagram ( $\log([\text{O III}]\lambda 5007/\text{H}\beta)$  versus  $\log([\text{N II}]\lambda 6584/\text{H}\alpha)$ ) for the SQ regions. Overplotted as grey continuous lines the predicted models from Allen et al. (2008) are shown for ionisation of gas considering fast shocks without precursor for solar metallicity and low density ( $n = 0.1 \text{ cm}^{-3}$ ), with velocities between 175 and  $1000 \text{ km s}^{-1}$ . The grey band in Fig. 7 corresponds to the mean uncertainties measured for the  $[\text{O III}]\lambda 5007/\text{H}\beta$  and  $[\text{N II}]\lambda 6584/\text{H}\alpha$  line ratios. As expected, the regions from NGC7319 nucleus appear in the AGN zone in the BPT diagram. The remaining SQ regions are displayed within the star-forming and composite (C) zones. We found 91 star-forming regions, 17 C regions, and 7 AGN-like regions. Rodríguez-Baras et al. (2014) found a fraction of pixels showing emission typical of the composite zone of the BPT diagram and claiming that HII regions can be found in the C zone (see also Sánchez et al. 2014). We believe that these C regions are contaminated by the emission of the shocked regions located in its vicinity.<sup>3</sup> Here, the SQ regions are classified as HII regions whenever they fulfill the two following conditions: i) located in the star-forming (SF) zone according to the Kauffmann demarcation or in the plotted grey band from Fig. 7; and ii) where the SNR for the  $\text{H}\alpha$ ,  $\text{H}\beta$ ,  $[\text{O III}]\lambda 5007$ , and  $[\text{N II}]\lambda 6584$  emission fluxes are higher than or equal to 3. AGN-like and composite regions are shown in several diagrams and maps. No values of SFR, nitrogen-to-oxygen abundance ratio (N/O) or oxygen abundance have been derived for composite or AGN-like regions.

In Fig. 8 (upper panel) we show the BPT map for the HV sub-sample. In the lower left panel, we present the BPT map for the

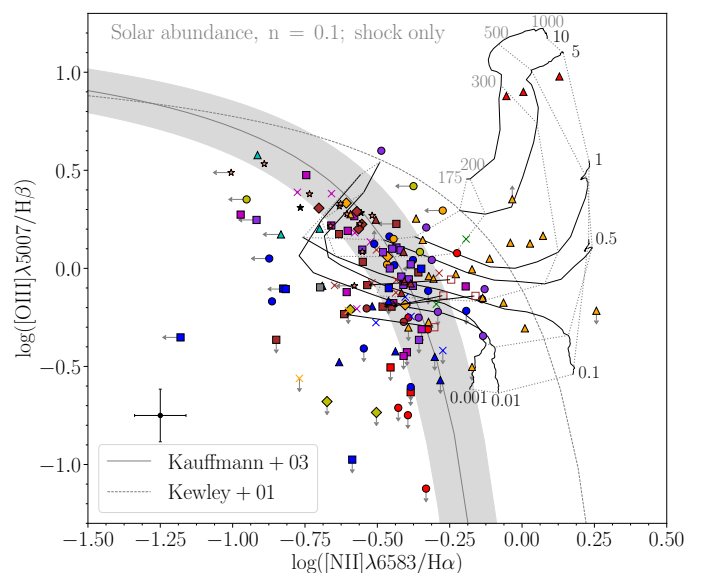


**Fig. 7.**  $[\text{O III}]\lambda 5007/\text{H}\beta$  versus  $[\text{N II}]\lambda 6584/\text{H}\alpha$  diagnostic diagram (BPT) for the SQ  $\text{H}\alpha$  emission regions. Regions without arrow have the SNR higher than 3 for the fluxes in the strong emission lines  $\text{H}\alpha$ ,  $\text{H}\beta$ ,  $[\text{O III}]\lambda 5007$ , and  $[\text{N II}]\lambda 6584$ , the typical error in each axis is represent with the black cross. Regions with ascending grey arrow have  $\text{SNR}(\text{H}\beta) < 3$ , regions with decreasing grey arrow have  $\text{SNR}([\text{O III}]\lambda 5007) < 3$ , while regions with grey arrow pointing left have  $\text{SNR}([\text{N II}]\lambda 6584) < 3$ . All the points in the figure have the same colours and markers as Fig. 3. The grey dashed line shows the Kewley et al. (2001) demarcation and the grey continuous line shows the Kauffmann et al. (2003) curve. The grey band shows the uncertainties for the BPT line ratios (i.e.  $[\text{O III}]\lambda 5007/\text{H}\beta$  and  $[\text{N II}]\lambda 6584/\text{H}\alpha$ ) to the Kauffmann demarcation. The black lines correspond to the shock only models of Allen et al. (2008) for solar metallicity and low density ( $n = 0.1 \text{ cm}^{-3}$ ), while the dotted lines correspond to the shock velocity.

LV sub-sample and in the lower right panel we display the three dimensional distribution of BPT class ( $\alpha$ ,  $\delta$ , radial velocity) for all the SQ regions. We colour-coded the SQ regions according to their position in the BPT diagram (see Fig. 7): i) star-forming regions (BPT colour bar equal to 1, blue regions); ii) C regions (BPT colour bar equal to 2, green regions); iii) AGN-like regions (BPT colour bar equal to 3, red regions). The LV map shows that all regions found in the SDR and NIs are star-forming. It is important to note that LSSR contaminates the NII spectra, where  $[\text{N II}]\lambda 6584$  from NII coincides in the same wavelength with  $\text{H}\alpha$  from the LSSR, and must be take into account when fitting the  $\text{H}\alpha$  and  $[\text{NII}]$  emission lines.<sup>4</sup> Also, all regions from NSQA, SSQA, L2, L4, and the northernmost regions (i.e. NW tidal) are star-forming regions. According to Fig. 7, most regions from L1 are compatible with the shock models adopted in this work. The HV map shows that all regions in the YTT and in SQA are star-forming regions. NG is a star-forming galaxy. Also, the regions found in the  $\text{H}\alpha$  ‘bridge’ are C and star-forming regions. As expected, NGC7319 presents AGN-like regions, but the North lobe presents star-forming and composite regions.

<sup>3</sup> Notice that  $[\text{N II}]\lambda 6584$  emission line is more sensitive to shocks and nonthermal processes than  $\text{H}\alpha$  emission line (Sulentic et al. 2001).

<sup>4</sup> This fact tell us that care should be exercised when analysing narrow-band photometric observations without spectroscopic information.

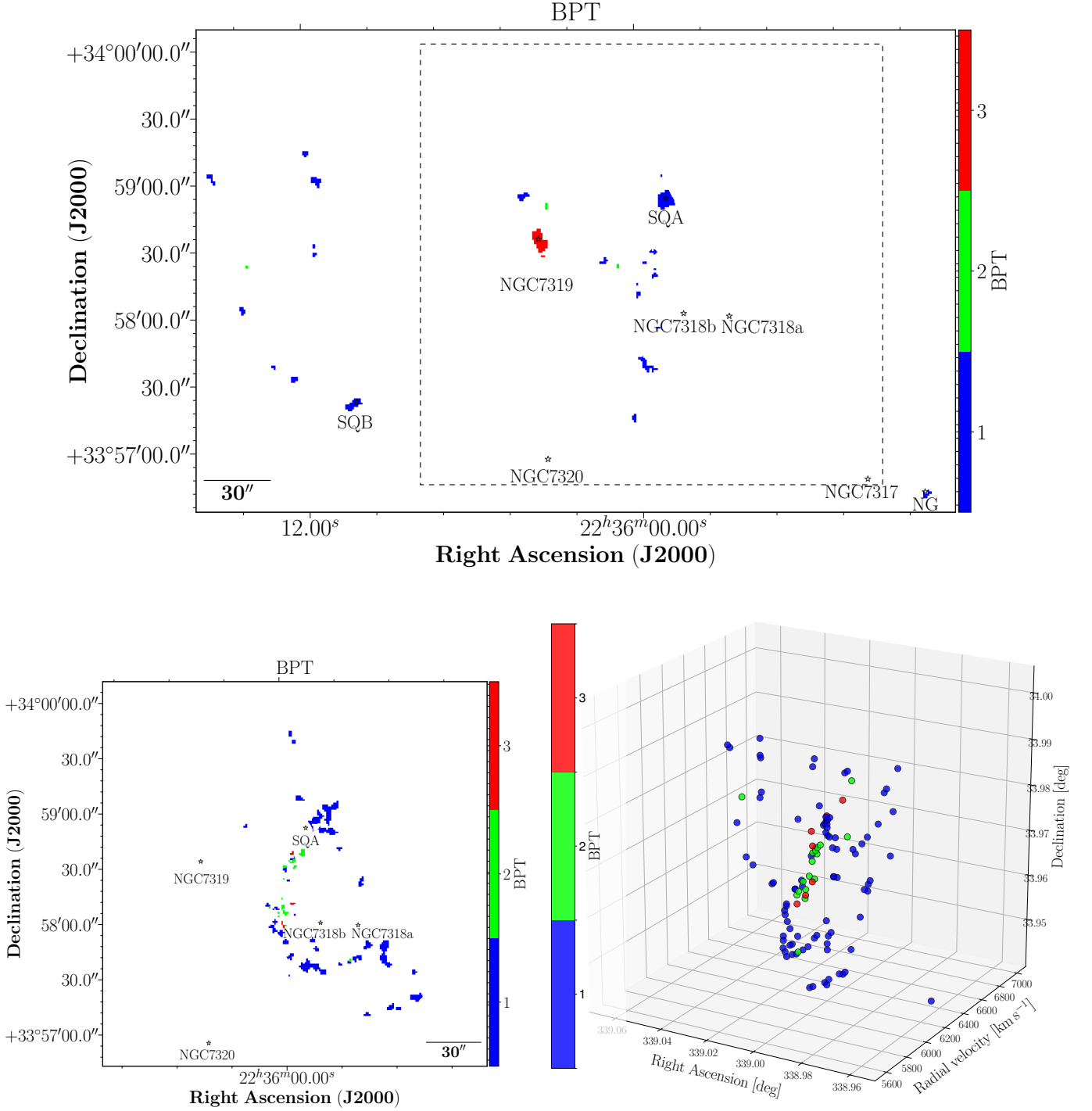


**Fig. 8.** SQ spatial map colour coded according to their position in the BPT diagnostic diagram for the HV sub-sample (upper panel), the LV sub-sample (lower left panel), and the three dimensional distribution of BPT class ( $\alpha$ ,  $\delta$ , radial velocity; lower right panel). Blue, green, and red pixels represent star-forming (1), composite (2), and AGN-like (3) regions, respectively.

#### 2.4. Derivation of the SFR and chemical abundances

Once we defined the star-forming objects among the sample of  $H\alpha$  emission regions in SQ, we derived the SFR, as well as the oxygen abundance and N/O. In order to derive the SFR, we use the following equation:

$$SFR(M_{\odot} \text{ yr}^{-1}) = 7.9 \times 10^{42} L_{H\alpha}(\text{erg s}^{-1}) \quad (1)$$

where  $L_{H\alpha} = 4\pi D^2 F(H\alpha)$  is the  $H\alpha$  luminosity corrected for reddening (see Sect. 2.1),  $D$  is the distance in Mpc (Kennicutt 1998), and  $F(H\alpha)$  is the  $H\alpha$  flux. We assume that the average distance of SQ is 88.6 Mpc (Hickson 1982; Mould et al. 2000; Fedotov et al. 2015). We computed the SFR for the 91 HII regions found in SQ according to the classification in Fig. 7. In Table C.2 we present the SFR values for each HII region. The HII regions from SQ

span  $\log(\text{SFR}/M_{\odot}\text{yr}^{-1})$  values between -3.26 (region 109) and -0.13 (region 122).

To derive the oxygen abundance, we use three empirical calibrators<sup>5</sup>: N2 (eq. 2) and O3N2 (eq. 3) from Pérez-Montero & Contini (2009), and R from Pilyugin & Grebel (2016), see eqs. 4 and 5. The R calibrator uses the line ratios N2, R2, and R3.<sup>6</sup>

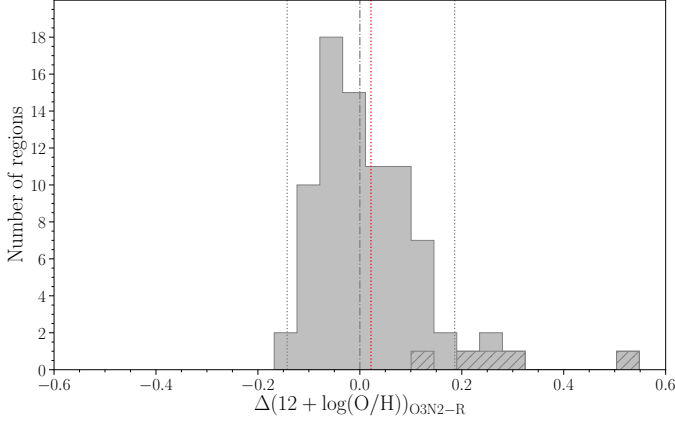


**Fig. 9.** Distribution of difference of the oxygen abundance derived with O3N2 and R calibrations for SQ HII regions. The grey dashed line indicates a difference equal to zero, and the red dashed line corresponds to the mean oxygen abundance difference between O3N2 and R calibrators (0.02 dex) for SQ HII regions; grey dotted lines indicate the  $3\sigma$  rms. The dashed histogram represents the sample of SQ HII regions when  $12 + \log(\text{O}/\text{H}) < 8.4$ , for which the R calibrator was adopted.

Pérez-Montero & Contini (2009) equations are:

$$12 + \log(\text{O}/\text{H}) = 0.79 \times \text{N2} + 9.07 \quad (2)$$

$$12 + \log(\text{O}/\text{H}) = 8.74 - 0.31 \times \text{O3N2} \quad (3)$$

where  $\text{N2} = \log([\text{N II}]\lambda 6584/\text{H}\alpha)$  and  $\text{O3N2} = \log([\text{O III}]\lambda 5007/\text{H}\beta \times \text{H}\alpha/[\text{N II}]\lambda 6584)$ , where  $\text{O3N2} < 2$ .

Pilyugin & Grebel (2016) equations are: if  $\log(\text{N2}) > -0.6$ :

$$12 + \log(\text{O}/\text{H}) = 8.589 + 0.022 \log\left(\frac{\text{R3}}{\text{R2}}\right) + 0.399 \log(\text{N2}) + \left(-0.137 + 0.164 \log\left(\frac{\text{R3}}{\text{R2}}\right) + 0.589 \log(\text{N2})\right) \times \log(\text{R2}) \quad (4)$$

on the contrary, if  $\log(\text{N2}) \leq -0.6$ :

$$12 + \log(\text{O}/\text{H}) = 7.932 + 0.944 \log\left(\frac{\text{R3}}{\text{R2}}\right) + 0.695 \log(\text{N2}) + \left(0.970 - 0.291 \log\left(\frac{\text{R3}}{\text{R2}}\right) - 0.019 \log(\text{N2})\right) \times \log(\text{R2}) \quad (5)$$

Figure 9 shows the distribution of difference between the O3N2 and R calibrators used to derive the oxygen abundance

<sup>5</sup> These are calibrated against direct derivations of abundances calculated with electron temperature measurements.

<sup>6</sup> We are aware that the derivation of oxygen abundance using bright-lines calibrators can be dependent on the particular indicator used. For the sake of the comparison with previous work, and taking into account the typical errors obtained, we selected these three calibrators for O/H.

for the sample of HII SQ regions.<sup>7</sup> The resulting oxygen abundances derived using both calibrators are consistent within errors when  $12 + \log(\text{O}/\text{H}) \geq 8.4$ , but not when  $12 + \log(\text{O}/\text{H}) < 8.4$ , a likely consequence of the range of validity adopted for the O3N2 parameter.<sup>8</sup> When  $12 + \log(\text{O}/\text{H}) < 8.4$ , we adopted the results from the R calibration (Pilyugin & Grebel 2016). For the sake of consistency, we used this last work to derive N/O (eq. 6) as:

$$\log(\text{N}/\text{O}) = -0.657 - 0.201 \log(\text{N2}) + (0.742 - 0.075 \log(\text{N2})) \times \log\left(\frac{\text{N2}}{\text{R2}}\right) \quad (6)$$

where:

$$\text{R2} = I([\text{O II}]\lambda\lambda 3727/I(\text{H}\beta)),$$

$$\text{N2} = I([\text{N II}]\lambda 6548 + \lambda 6584/I(\text{H}\beta) = 1.333I([\text{N II}]\lambda 6584/I(\text{H}\beta)), \quad (7)$$

$$\text{R3} = I([\text{O III}]\lambda 4959 + \lambda 5007/I(\text{H}\beta) = 1.333I([\text{O III}]\lambda 5007/I(\text{H}\beta)).$$

In Table C.2 we show several properties derived in this section. In Col. 1 the region name is presented. Cols. 2 and 3 present the SFR and  $\text{H}\alpha$  luminosity. Col. 4 shows the classification according to the BPT diagram. Col. 5 tells us whether the velocity of the region belongs to the LV (0 in the column) or HV (1 in the column).

In Table C.3 we show the O/H and N/O values for the SQ HII regions derived in this section. In Col. 1 the region name is presented. Cols. 2, 3, and 4 show the oxygen abundances using N2, O3N2, and R calibrators, respectively. Col. 5 displays the N/O using Pilyugin & Grebel (2016). Col. 6 tells us whether the velocity of the region belongs to the LV (0 in the column) or HV (1 in the column) sub-samples.

## 2.5. Spatially resolved analysis of SFR, O/H and N/O

In order to study the provenance of the gas it is necessary to carry out a comprehensive study of the spectroscopic information presented in the previous sections. Consequently, in Sect. 2.4 we derived the SFR, as well as the oxygen abundance and N/O for our sample of HII SQ regions.

Figure 10 shows the SFR map for the SQ. Upper panel presents HII regions belonging to the LV sub-sample, while the lower panel shows regions from the HV sub-sample. The HII regions from SQ, except SQA and SQB, have  $\log(\text{SFR}/M_{\odot}\text{yr}^{-1})$  lower than -1. It can be seen that the regions from Shs, NW tidal tail, L1, L2, and L4 have a quite low SFR ( $\log(\text{SFR}/M_{\odot}\text{yr}^{-1}) < -2$ ). Moreover, NIs, SDR, Hs, NSQA, SSQA, and the North lobe have a low SFR ( $\log(\text{SFR}/M_{\odot}\text{yr}^{-1}) < -1$ ). Conversely, SQA has the greatest SFR value found in the SQ ( $\log(\text{SFR}/M_{\odot}\text{yr}^{-1}) \sim 0.06$ ). SQB also has a SFR higher than the average SFR found in SQ (region 15,  $\log(\text{SFR}/M_{\odot}\text{yr}^{-1}) \sim 0.7$ ). On average, the HII regions from YTTs have higher SFR values than YTTN ( $\log(\text{SFR}/M_{\odot}\text{yr}^{-1}) = -1.5$  versus -2, respectively). NG has a value of  $\log(\text{SFR}/M_{\odot}\text{yr}^{-1}) = -1$  and the North lobe has  $\log(\text{SFR}/M_{\odot}\text{yr}^{-1}) \sim -1.5$ .

In Fig. 11 we show the oxygen abundance maps for LV (upper panel) and HV (lower panel) sub-samples using the O3N2

<sup>7</sup> For 10 HII regions for which no  $[\text{O II}]\lambda 3727$  was measured the R calibrator cannot be used.

<sup>8</sup> A similar situation holds for N2.

calibrator from Pérez-Montero & Contini (2009). In the App. B we show the oxygen abundance maps using the R calibrator from Pilyugin & Grebel (2016). As we explained in Sect. 2.4, the oxygen abundance calibrators (O3N2 and R) are consistent when  $12+\log(\text{O}/\text{H})\geq 8.4$ , and either can be adopted; and when  $12+\log(\text{O}/\text{H})< 8.4$ , we used the results from the R calibrator. In general, the two metallicity maps for the LV sub-sample show similar trends regardless of the calibrator used. On average, NIs spans metallicity values from solar ( $12+\log(\text{O}/\text{H})=8.69$ ) to half-solar ( $12+\log(\text{O}/\text{H})=8.4$ ). The regions from the NI1 and NI2 zones, which coincide with the pointings in Iglesias-Páramo et al. (2012), show oxygen abundance values in the range of 8.5 to 8.66, in accordance with Iglesias-Páramo et al. (2012). Also, SDR has an average metallicity of  $12+\log(\text{O}/\text{H})\sim 8.45$  but the minimum value calculated in this zone is 8.3 (region 172); moreover, regions from the tidal tail NW present metallicity values close to  $12+\log(\text{O}/\text{H})=8.45$  (regions 97 and 82, respectively), in agreement with de Mello et al. (2012). As we can see in Fig. 11 and Table C.3, NSQA has slightly higher metallicity values than SSQA (8.69 compared to 8.6), on average. The two HII regions from L2 (we recall that this zone connect NSQA with SSQA) present a metallicity of  $12+\log(\text{O}/\text{H})\sim 8.57$ , as well as L4 zone. On the other hand, when we focus on the HV sub-sample (lower panel in Fig. 11) we can see that SQA, the region 10 (in YTTN), and region 2 (in YTTS) show the lower values of metallicity ( $12+\log(\text{O}/\text{H})=8.4$  on average), where SQB has  $12+\log(\text{O}/\text{H})=8.5$ . For NG we found  $12+\log(\text{O}/\text{H})=8.27$ . The HII regions from Shs spans metallicity values between  $8 < 12+\log(\text{O}/\text{H}) < 8.7$ . Moreover, the regions from YTT present metallicity values from  $12+\log(\text{O}/\text{H})=8.2$  (region 2) to solar metallicity (region 14), in agreement with Mendes de Oliveira et al. (2004). We found oversolar metallicity values in the North lobe and in region 35 (H $\alpha$  'bridge'). The average metallicity derived in SQ is  $\langle 12 + \log(\text{O}/\text{H}) \rangle = 8.6$ , and the minimum value found is  $12+\log(\text{O}/\text{H})=8.0$  (region 59).

In Fig. 12 we show the N/O maps for LV (upper panel) and HV (lower panel) sub-samples of SQ HII regions. In this work, we used the calibrator from Pilyugin & Grebel (2016) as the representative N/O for each HII region. It is important to note that the regions found in HV sub-sample have lower values of N/O than those located in LV ( $\log(\text{N}/\text{O})=-1$  and  $-0.86$ , respectively). The average value of N/O derived in SQ is  $-0.88$ . Except in the North lobe, on average the remaining HII regions in the HV sub-sample have subsolar N/O values.<sup>9</sup> However, in the LV sub-sample, we found two regions with subsolar N/O values (SSQA and NW with mean values of  $\log(\text{N}/\text{O})=-0.93$  and  $-0.97$ , respectively). This may indicate that both parts have different behaviour coming from diverse galaxies. LV could come from NGC7318B, whilst HV could come from NGC7319 and the debris produced in any past interaction between NGC7319 and other galaxies (e.g. NGC7317, NGC7318A, or NGC7320c). Only 6 out of 54 HII regions with N/O in the LV sub-sample have values  $\log(\text{N}/\text{O}) < -1$  (regions 50, 65, 82, 147, 173, and 174). No evidence of a N/O gradient is found in NIs ( $\sim$ solar value, see Sect 3). NSQA presents higher values than SSQA on average ( $\log(\text{N}/\text{O})=-0.8$  and  $-1$ , respectively). We can divide NSQA in two parts, East and West. The eastern part has lower N/O values than the western part ( $\log(\text{N}/\text{O})=-0.9$  versus  $\gtrsim -0.75$ ). The SDR zone on average presents the same N/O as NI5. However, except the North lobe ( $\log(\text{N}/\text{O})=-0.64$ ), all zones from the HV sub-sample have  $\log(\text{N}/\text{O})\lesssim -1$ . Only 7 out of 33 HII regions with N/O in the HV sub-sample have  $\log(\text{N}/\text{O}) > -0.86$  (regions

11, 13, 14, 15, 24, 64, and 77). Additionally, NG has a low value of  $\log(\text{N}/\text{O})=-1.3$ . The minimum value for N/O in SQ is  $\log(\text{N}/\text{O})=-1.6$  (region 59).

<sup>9</sup>  $\log(\text{N}/\text{O})_{\odot} = -0.86$  (Asplund et al. 2009; Tsamis et al. 2011).

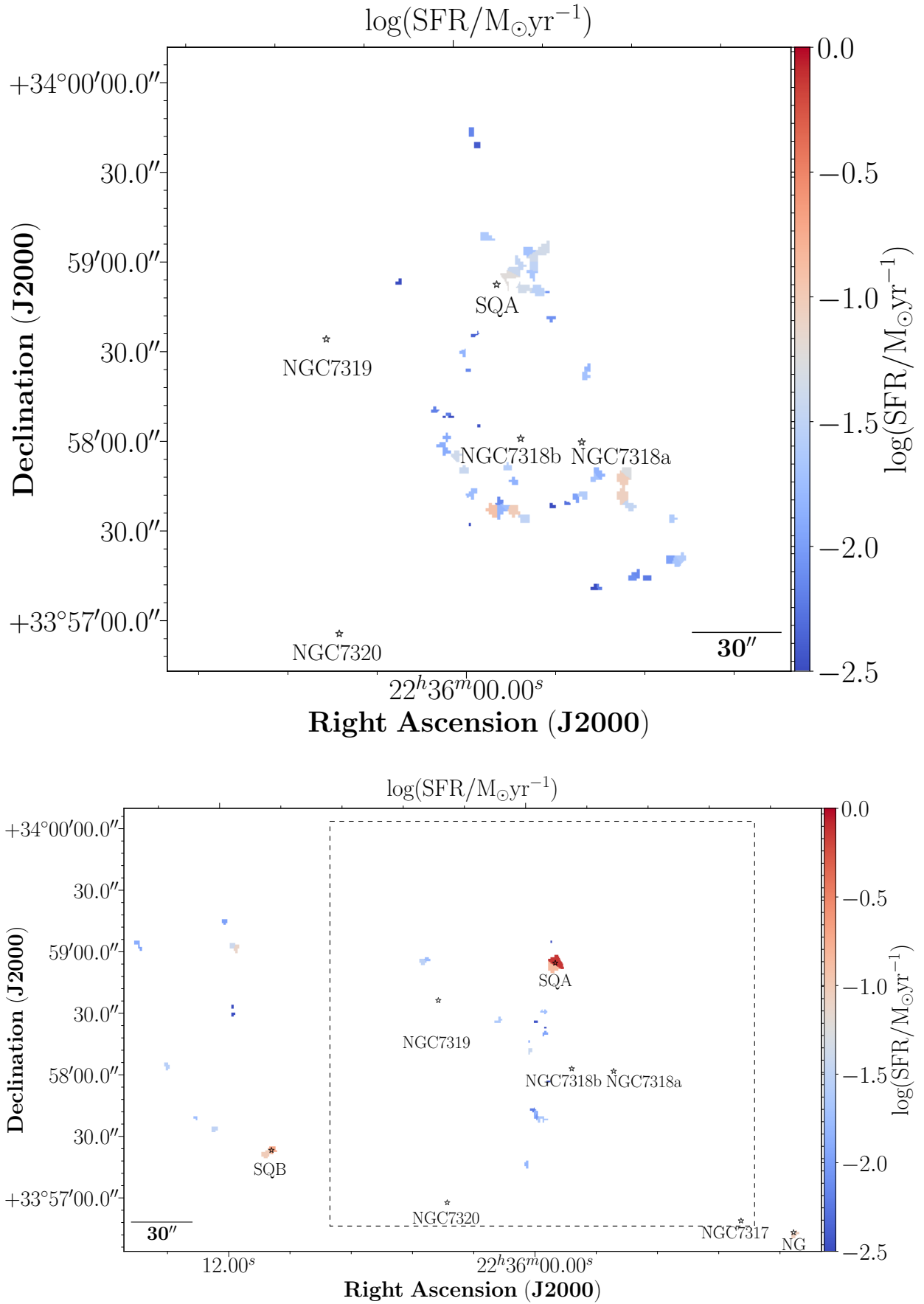


**Fig. 10.** SQ spatial map colour coded according to their SFR for the LV sub-sample (upper panel) and the HV sub-sample (lower panel).

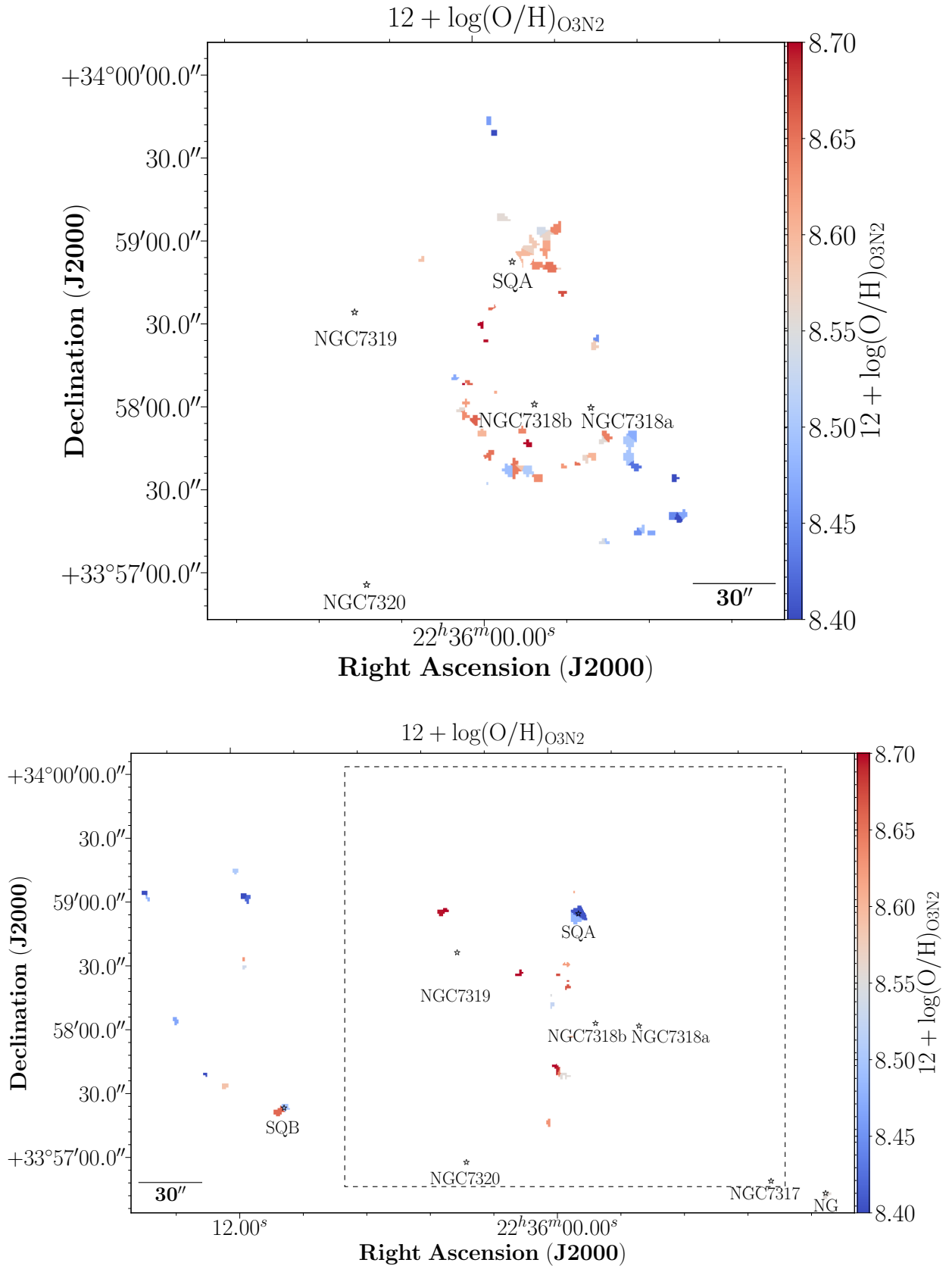


**Fig. 11.** SQ spatial map for the LV sub-sample (upper panel) and the HV sub-sample (lower panel) colour coded according to their  $12 + \log(\text{O}/\text{H})$  derived using the O3N2 calibrator from Pérez-Montero & Contini (2009).

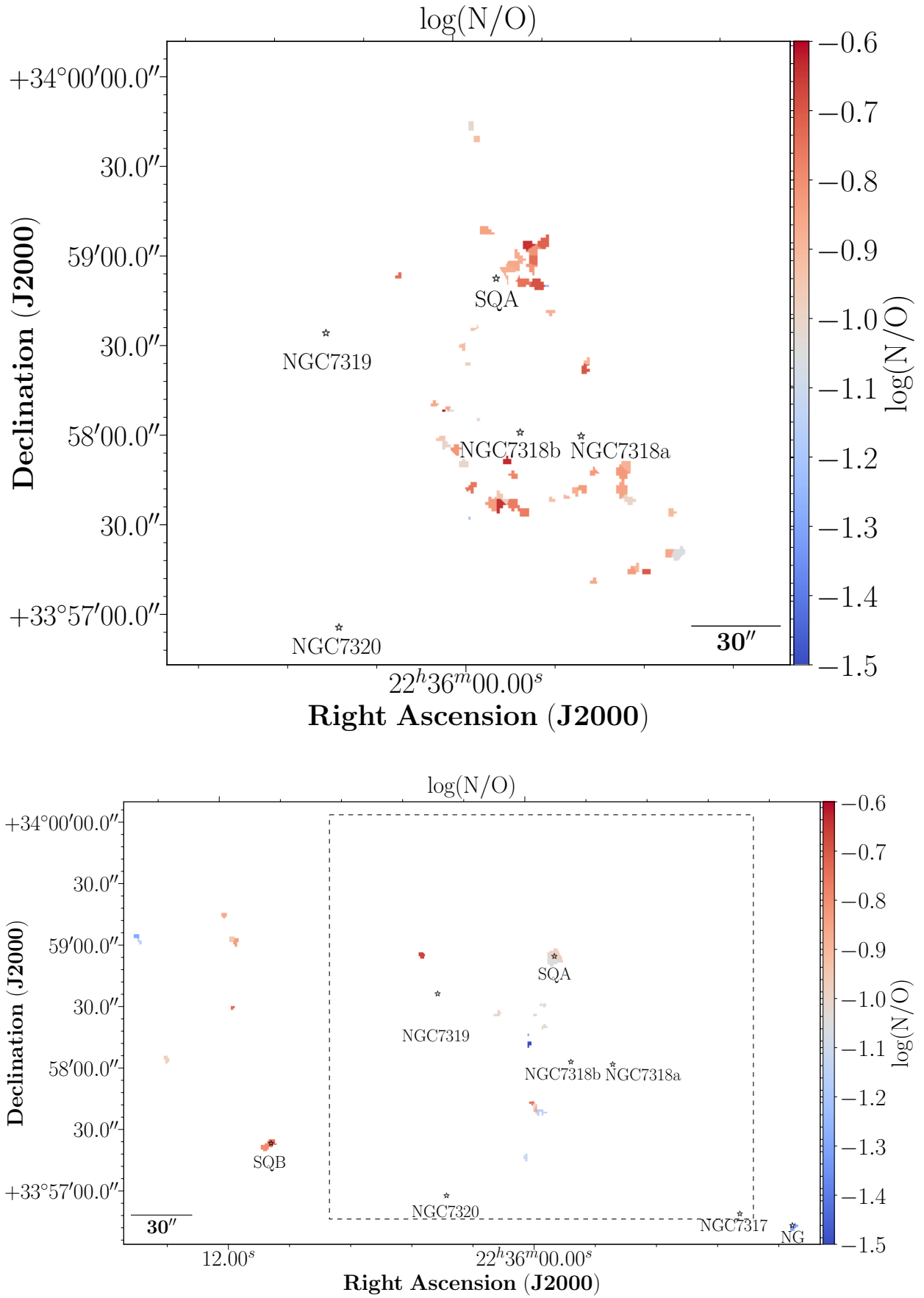


**Fig. 12.** SQ spatial map for the LV sub-sample (upper panel) and the HV sub-sample (lower panel) colour coded according to their  $\log(\text{N/O})$  derived from Pilyugin & Grebel (2016) calibrator.

### 3. Discussion and summary

A sample of 175 SQ H $\alpha$  emitting regions, 22 of them presenting two velocity components, was defined according to the following criteria: i) the velocity of the region is within the velocity range of SQ (between  $\sim 5500$  and  $\sim 7000$  km s $^{-1}$ ); ii) the detection of at least one additional emission line beside H $\alpha$ . We selected the SF regions from the BPT diagram. Taking this into account, we found 91 HII regions, 17 composite, and 7 AGN-like regions. We found all composite and AGN regions in the LV sub-sample, located in the L1, SSQA, Shs, and North lobe zones. This is also confirmed by the  $\log([\text{N II}]\lambda 6584/\text{H}\alpha)$  versus radial velocity diagram. We need to keep in mind that the spectra from NII are contaminated by the shock zone, since the  $[\text{N II}]\lambda 6584$  from NII coincides in wavelength with the H $\alpha$  from the shock. It is important to correct for this in order not to find HII regions in the composite zone (e.g. Rodríguez-Baras et al. 2014) to avoid misclassifications.

We found three AGN-like spectra in the L1 zone and another one in NSQA. As expected, the NGC7319 nucleus has AGN classification, but the North lobe presents also star-forming and composite regions. The composite and AGN regions are in L1, SSQA, and Shs, being consistent with fast shock ionisation without precursor for solar metallicity and low density ( $n = 0.1$  cm $^{-3}$ ), with velocities between 175 and 300 km s $^{-1}$  using the models from Allen et al. (2008). The star-forming regions are located in the North and South zone of the shock (NW-LV, NW-HV, and SW zones in Williams et al. 2002), where there is HI. Conversely, the regions in the YTT, the new intruder (NI, NGC7318B) and SDR are star-forming.

We derived the total SFR for the sample of 91 HII regions in SQ. The total SFR found for SQ is  $\log(\text{SFR}/M_{\odot} \text{ yr}^{-1})=0.496$ . 55% of the SFR ( $\log(\text{SFR}/M_{\odot} \text{ yr}^{-1})=0.24$ ) comes from the HV sub-sample, while the LV sub-sample is 45% ( $\log(\text{SFR}/M_{\odot} \text{ yr}^{-1}) = 0.15$ ). 28% of the total SFR in SQ comes from SQA ( $\log(\text{SFR}/M_{\odot} \text{ yr}^{-1})=-0.06$ ), while 9% ( $\log(\text{SFR}/M_{\odot} \text{ yr}^{-1})=-0.54$ ) is in SQB. So, except for SQA and SQB, the material prior to the collision with NI does not show a high SFR, therefore SQ was apparently quench. There are differences between the SFR derived for SQA from Xu et al. (2005) and the one derived here. The difference is likely due to the fact that Xu et al. (2005, see region VI) derives the SFR for a larger area which includes SQA, NSQA, L2, and H1. When considering all this zones we obtained  $\log(\text{SFR}/M_{\odot} \text{ yr}^{-1})=0.12$ , which is in agreement with Xu et al. (2005), that found  $\log(\text{SFR}/M_{\odot} \text{ yr}^{-1})=0.125$ .

Fig. 13 shows the relation between  $A_v$  and SFR for the sample of 91 SQ HII regions (upper panel) and for the sample of 209276 Sloan Digital Sky Survey (SDSS) star-forming galaxies corrected for aperture effects<sup>10</sup> from Duarte Puertas et al. (2017). We show that, in both SQ HII regions and SDSS star-forming galaxies, the extinction is correlated with the SFR, in such a way that the higher the SFR, the higher the extinction (with their dispersion), and spread the same range of  $A_v$  values. Therefore, the most massive galaxies and regions present more extinction. For the 91 SQ HII regions, we parameterised the correlation between SFR and  $A_v$  by using Pearson's coefficient. We have found that it is a moderate positive correlation (0.5). It can be expected that the SQ HII regions are shifted in this diagram since they have lower SFR values. In the SDSS star-forming galaxies, each extended galaxy is considered as a single point in the  $A_v$  versus

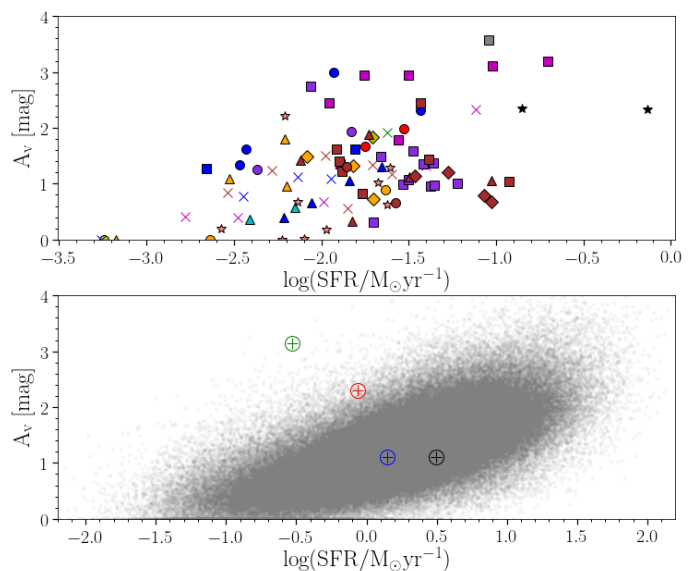


**Fig. 13.** Relation between  $A_v$  and SFR for: Upper panel) the 91 SQ HII regions, all the points in the figure have the same colours and markers as Fig. 3; and Lower panel) a sample of 209276 SDSS star-forming galaxies corrected for aperture effects found in Duarte Puertas et al. (2017). Black, blue, red, and green  $\oplus$  represent the position of the total SFR and the mean  $A_v$  for all the SQ HII regions, NI, SQA, and SQB respectively. Grey points show the values for the sample of 209276 SDSS star-forming galaxies.

SFR diagram. We note that when considering normal galaxies (i.e. not reduced to a single point) the gas is concentrated in the central zones whilst in SQ the gas is not located in the central areas of the galaxies. In our case, when we considered the total SFR and the  $A_v$  median for all SQ and NI, both are located in the same part as the footprint of SDSS star-forming galaxy. On the one hand, we can appreciate that both SQA and SQB are outliers in this diagram, since they have more  $A_v$  than galaxies with the same SFR. Besides, the SQ HII regions are displaced elsewhere since there is an interaction and, thus, their position depends on whether the HI gas is moving or not. The regions with more extinction and SFR are outside the galaxies because the interactions have dispersed the gas to the peripheral zones. Henceforth, the extinction in the SQ HII regions does not follow the general trend observed in spiral galaxies. Generally, the inner-outer diminishing extinction pattern that occurs in spiral galaxies disappears giving rise to a trend dominated by the successive interactions. All above is in accordance with the interpretation of Verdes-Montenegro et al. (2001) about the distribution of HI in compact groups. SQ is part of Phase 3a according to the evolutionary sequence from the HI distribution of Verdes-Montenegro et al. (2001). They say that the HI has been stripped out entirely, or almost, in this Phase from the disc of the galaxies that belong to the compact groups, suggesting that the HI could be found in the tails produced by the interactions that the galaxies suffered.

The analysis of the chemical abundances of oxygen and N/O for our sample of SQ HII regions shows that the range of oxygen abundance and N/O are between solar and a fourth of solar approximately. The lowest values are found in the region 59b ( $12+\log(\text{O}/\text{H})\approx 8$  and  $\log(\text{N}/\text{O})\approx -1.6$ ). Figure 14 shows the relation between metallicity (upper panels) or N/O (left lower panel) and the radial velocity for the sample of HII SQ regions. Also, in the right lower panel, we show the relation between  $A_v$  and the

<sup>10</sup> The total SFR for the SDSS star-forming galaxies was derived using the empirical aperture corrections based on the Calar Alto Legacy Integral Field Area (CALIFA) survey defined by Iglesias-Páramo et al. (2013, 2016).

radial velocity for all the SQ emission regions. The presence of an inner-outer radial metallicity gradient along the tail is clearly visible for NIs and it will be commented on below. The YTT presents a median oxygen abundance of  $\sim 8.55$  that agrees with [Mendes de Oliveira et al. \(2004\)](#). In the case of the regions in NSQA, a hint for the existence of a radial variation of the oxygen abundance and N/O ratio has been seen, though the complexity of this system prevents us from associating this variation with a spiral arm.

The SQ HII regions are mostly metal-rich ( $12+\log(\text{O}/\text{H}) \gtrsim 8.5$ ). All 8 metal-poor regions found here are located in the HV sub-sample and none in the LV sub-sample. In the case of the N/O, we found 10 regions with  $\log(\text{N}/\text{O})$  lower than half solar value. Ninety percent of the regions with  $\text{N}/\text{O} \leq \frac{1}{2}(\text{N}/\text{O})_{\odot}$  are located in the HV sub-sample. All the regions in the LV sub-sample (except one) have  $\log(\text{N}/\text{O})$  values higher than half solar. This might indicate that at least two chemically different gas components cohabit in SQ, one metal-rich in the LV sub-sample and in most regions of YTT, and one metal-poor in LSSR and in few YTT regions.

The oxygen abundance values obtained from the empirical calibrations for the SQ HII regions were compared with the predictions of theoretical models from `HIICHEMISTRY` ([Pérez-Montero 2014](#)). Consistency has been found between the theoretical and empirical oxygen abundances within the errors. The mean of the O/H differences between O3N2 and `HIICHEMISTRY` abundance derivations is found to be  $-0.05$  dex, with a  $1\sigma$  rms of 0.05 dex. A similar comparison carried out between R and `HIICHEMISTRY` O/H derivations gives a mean value of the difference of  $-0.07$  dex, with a  $1\sigma$  rms of 0.11 dex. As for the N/O ratio, the distribution of the differences between N/O from [Pilyugin & Grebel \(2016\)](#) and from `HIICHEMISTRY` gives a mean of  $-0.19$  dex, with a  $1\sigma$  rms of 0.10 dex.

In this work, we studied the radial gradients for several properties of the spiral arm associated with the NIs (i.e. NI1, NI2, NI4, and NI5 strands) and SDR. Taking into account that the distance of SQ is 88.6 Mpc, we defined the distance  $d$  as the projected distance from one region to the next, and  $d_{max}$  as the projected distance between the first region (the northernmost region of NI1, #46) to the last region (#172). As we can see in [Fig. 15](#), the oxygen abundance in NI1, NI2, and NI4 appears to be constant. This is compatible with the results found in a spiral arm at a constant distance from the nucleus. Then, the metallicity value decreases as we approach the NI5 and SDR regions. We found a similar result when we studied  $\log([\text{N II}]\lambda 6584/\text{H}\alpha)$ . We did not find a N/O gradient, because the values are almost constant (solar value). Thus, the metal-rich material should come from the inner part of the galaxy. In the case of the ratio  $\log([\text{O III}]/\text{H}\beta)$ , we found lower values in NI1 than in SDR. We obtained an  $A_v$  gradient with higher values in NI1 than in SDR. All the properties studied in [Fig. 15](#) are consistent with the presence of inner-outer variation along the NI tails in the line of the results obtained by [Iglesias-Páramo et al. \(2012\)](#) and [Rodríguez-Baras et al. \(2014\)](#). Finally, the relation between  $\log(\text{N}/\text{O})$  and  $12+\log(\text{O}/\text{H})$  for the SQ HII region is presented in [Fig. 16](#). A secondary production of nitrogen can be seen in the behaviour of the relation between  $\log(\text{N}/\text{O})$  and  $12+\log(\text{O}/\text{H})$  for the HII regions belonging to the arms. In [Fig. 16](#) we can see that almost ten HII regions present metallicity similar to that of the Large Magellanic Cloud ( $12+\log(\text{O}/\text{H}) \lesssim 8.45$ ), and  $\log(\text{N}/\text{O})$  values typical of regions belonging to the outer part of galactic discs ( $\log(\text{N}/\text{O}) \lesssim -1$ ). Further deep and higher spectral observations will help to understand the nature of the different chemical, kinematical, and structural components unveiled in this work.

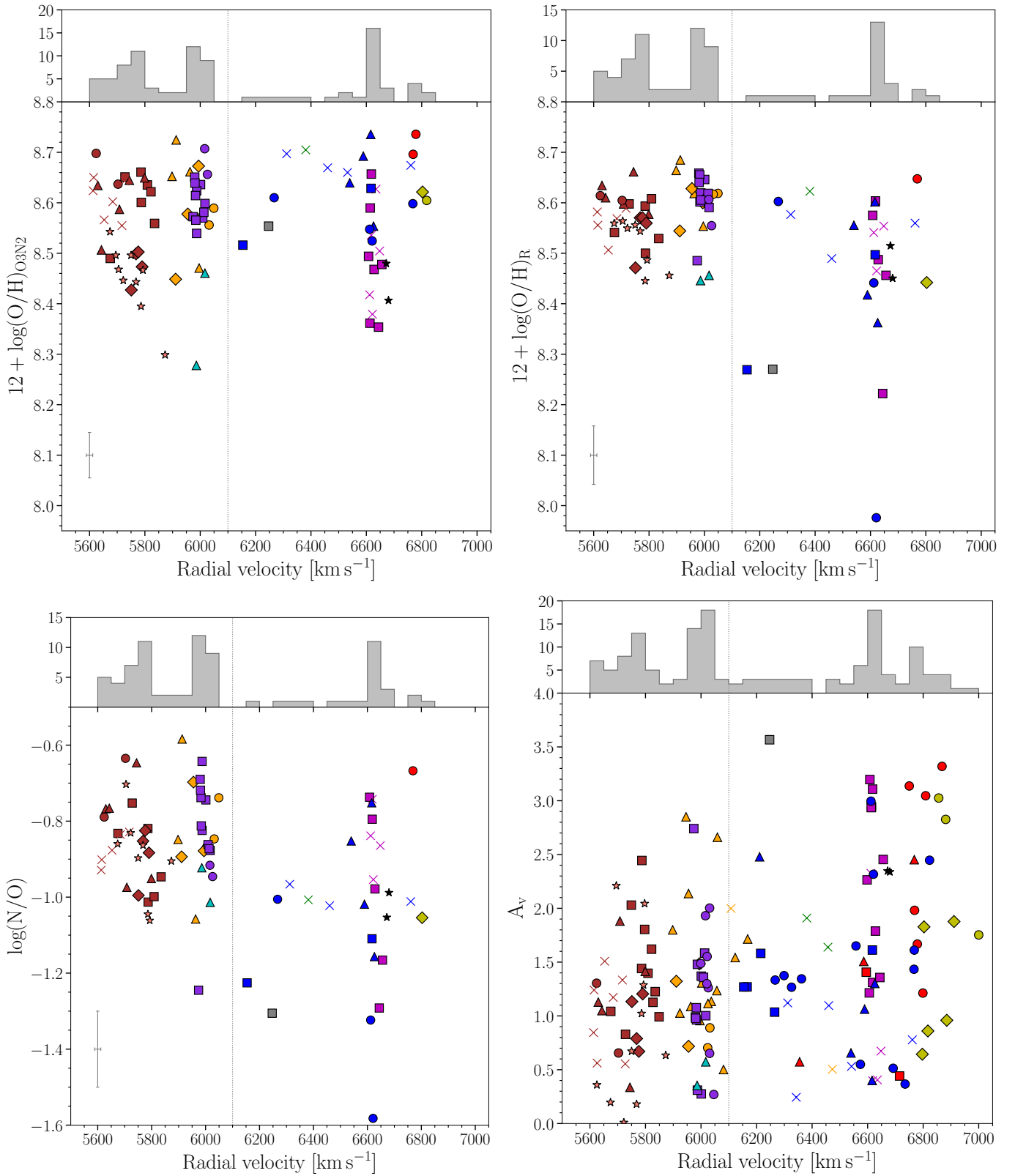


**Fig. 14.** i) upper left panel: Relation between  $12 + \log(\text{O}/\text{H})_{\text{O3N2}}$  and radial velocity for the HII regions; ii) upper right panel: Relation between  $12 + \log(\text{O}/\text{H})_R$  and radial velocity for the HII regions; iii) lower left panel: Relation between  $\log(\text{N}/\text{O})$  and radial velocity for the HII regions; iv) lower right panel: Relation between  $A_v$  and radial velocity for the  $\text{H}\alpha$  emission regions. All the points in the figures have the same colours and markers as Fig. 3. The vertical black dashed line corresponds to the value at radial velocity =  $6100 \text{ km s}^{-1}$ . Above each figure its distribution of the radial velocity for the SQ HII regions is represented. The lower left crosses indicate the typical error of the two parameters.

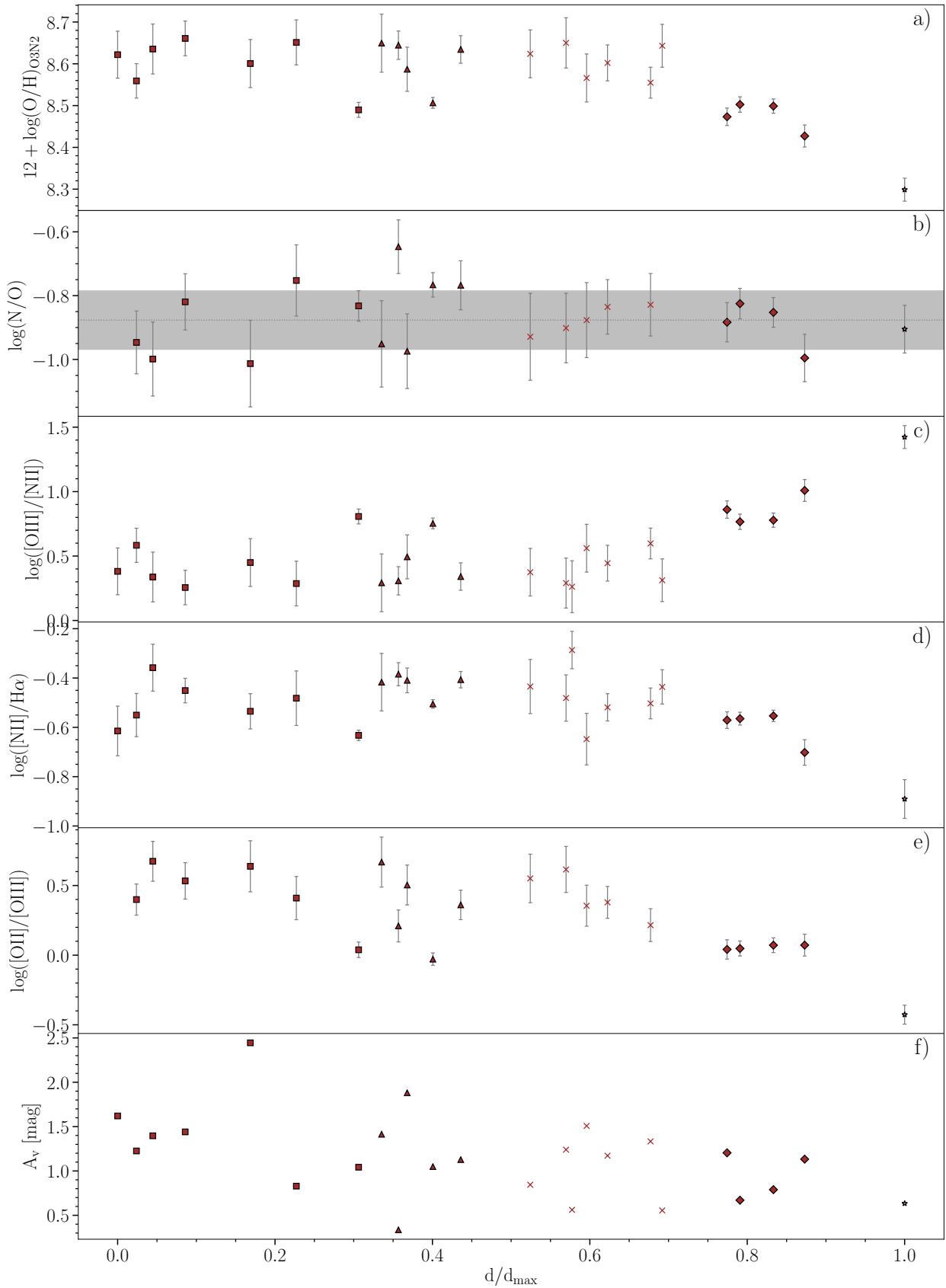


**Fig. 15.** From top to bottom: Radial gradients for  $12 + \log(\text{O}/\text{H})$ ,  $\log(\text{N}/\text{O})$ ,  $\log([\text{O III}]/[\text{N II}])$ ,  $\log([\text{N II}]/\text{H}\alpha)$ ,  $\log([\text{O II}]/[\text{O III}])$ , and  $A_v$  along the NI tails.

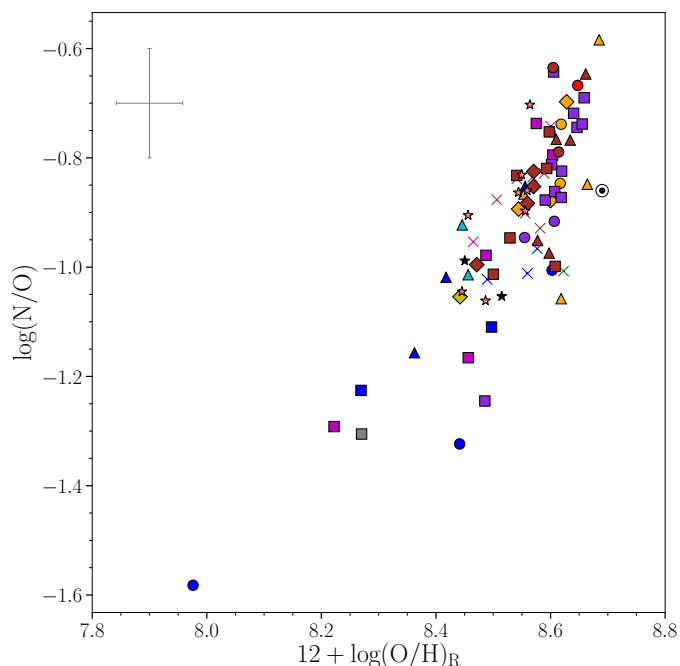


**Fig. 16.** Relation between  $\log(N/O)$  and  $12 + \log(O/H)_R$ . All the points in the figures have the same colours and markers as Fig. 3. The upper left cross indicates the typical error of both parameters. The marker  $\circ$  shows the position of the solar value in this diagram.

*Acknowledgements.* Based on observations obtained with SITELLE, a joint project of Université Laval, ABB, Université de Montréal, and the Canada-France-Hawaii Telescope (CFHT), which is operated by the National Research Council of Canada, the Institut National des Sciences de l'Univers of the Centre National de la Recherche Scientifique of France, and the University of Hawaii. The authors wish to recognise and acknowledge the very significant cultural role that the summit of Mauna Kea has always had within the indigenous Hawaiian community. We are most grateful to have the opportunity to conduct observations from this mountain. SDP, JVM, JIP, CK, EPM, and AAP acknowledge financial support from the Spanish Ministerio de Economía y Competitividad under grants AYA2013-47742-C4-1-P and AYA2016-79724-C4-4-P, from Junta de Andalucía Excellence Project PEX2011-FQM-7058, and also acknowledge support from the State Agency for Research of the Spanish MCIU through the 'Center of Excellence Severo Ochoa' award for the Instituto de Astrofísica de Andalucía (SEV-2017-0709). LD is grateful to the Natural Sciences and Engineering Research Council of Canada, the Fonds de Recherche du Québec, and the Canada Foundation for Innovation for funding.

This research made use of Python (<http://www.python.org>) and IPython (Pérez & Granger 2007); APLpy (Robitaille & Bressert 2012); Numpy (Van Der Walt et al. 2011); Pandas (McKinney 2010); of Matplotlib (Hunter 2007), a suite of open-source Python modules that provides a framework for creating scientific plots. This research made use of Astropy, a community-developed core Python package for Astronomy (Astropy Collaboration et al. 2013). The Astropy web site is <http://www.astropy.org>. This research made use of astrodendro, a Python package to compute dendrograms of astronomical data (<http://www.dendrograms.org/>)

## References

Allen, M. G., Groves, B. A., Dopita, M. A., Sutherland, R. S., & Kewley, L. J. 2008, *ApJS*, 178, 20  
 Allen, R. J. & Hartsuiker, J. W. 1972, *Nature*, 239, 324  
 Alloin, D., Collin-Souffrin, S., Joly, M., & Vigroux, L. 1979, *A&A*, 78, 200  
 Asplund, M., Grevesse, N., Sauval, A. J., & Scott, P. 2009, *ARA&A*, 47, 481  
 Astropy Collaboration, Robitaille, T. P., Tollerud, E. J., et al. 2013, *A&A*, 558, A33  
 Baldwin, J. A., Phillips, M. M., & Terlevich, R. 1981, *PASP*, 93, 5  
 Berg, D. A., Skillman, E. D., Marble, A. R., et al. 2012, *ApJ*, 754, 98  
 Cardelli, J. A., Clayton, G. C., & Mathis, J. S. 1989, *ApJ*, 345, 245

Croxall, K. V., van Zee, L., Lee, H., et al. 2009, *ApJ*, 705, 723  
 de Mello, D. F., Urrutia-Viscarra, F., Mendes de Oliveira, C., et al. 2012, *MNRAS*, 426, 2441  
 Díaz, A. I., Castellanos, M., Terlevich, E., & Luisa García-Vargas, M. 2000, *MNRAS*, 318, 462  
 Drissen, L., Martin, T., Rousseau-Nepton, L., et al. 2019, *MNRAS*, 485, 3930  
 Duarte Puertas, S., Iglesias-Páramo, J., Vilchez, J. M., et al. 2019, *A&A*, 629, A102  
 Duarte Puertas, S., Vilchez, J. M., Iglesias-Páramo, J., et al. 2017, *A&A*, 599, A71  
 Duc, P.-A., Cuillandre, J.-C., & Renaud, F. 2018, *MNRAS*, 475, L40  
 Duc, P.-A., Paudel, S., McDermid, R. M., et al. 2014, *MNRAS*, 440, 1458  
 Fedotov, K., Gallagher, S. C., Durrell, P. R., et al. 2015, *MNRAS*, 449, 2937  
 Fedotov, K., Gallagher, S. C., Konstantopoulos, I. S., et al. 2011, *AJ*, 142, 42  
 Grandmont, F., Drissen, L., Mandar, J., Thibault, S., & Baril, M. 2012, in *Society of Photo-Optical Instrumentation Engineers (SPIE) Conference Series*, Vol. 8446, Proc. SPIE, 84460U  
 Hickson, P. 1982, *ApJ*, 255, 382  
 Hunter, J. D. 2007, *Computing In Science & Engineering*, 9, 90  
 Iglesias-Páramo, J., López-Martín, L., Vilchez, J. M., Petropoulou, V., & Sulentic, J. W. 2012, *A&A*, 539, A127  
 Iglesias-Páramo, J., Vilchez, J. M., Galbany, L., et al. 2013, *A&A*, 553, L7  
 Iglesias-Páramo, J., Vilchez, J. M., Rosales-Ortega, F. F., et al. 2016, *ApJ*, 826, 71  
 Kauffmann, G., Heckman, T. M., Tremonti, C., et al. 2003, *MNRAS*, 346, 1055  
 Kennicutt, Jr., R. C. 1998, *ARA&A*, 36, 189  
 Kewley, L. J., Dopita, M. A., Sutherland, R. S., Heisler, C. A., & Trevena, J. 2001, *ApJ*, 556, 121  
 Konstantopoulos, I. S., Appleton, P. N., Guillard, P., et al. 2014, *ApJ*, 784, 1  
 Lee-Waddell, K., Madrid, J. P., Spekkens, K., et al. 2018, *MNRAS*, 480, 2719  
 Lelli, F., Duc, P.-A., Brinks, E., et al. 2015, *A&A*, 584, A113  
 Lisenfeld, U., Braine, J., Duc, P.-A., et al. 2002, *A&A*, 394, 823  
 Martin, T., Drissen, L., & Joncas, G. 2015, in *Astronomical Society of the Pacific Conference Series*, Vol. 495, *Astronomical Data Analysis Software and Systems XXIV (ADASS XXIV)*, ed. A. R. Taylor & E. Rosolowsky, 327  
 McKinney, W. 2010, in *Proceedings of the 9th Python in Science Conference*, ed. S. van der Walt & J. Millman, 51 – 56  
 Mendes de Oliveira, C., Cypriano, E. S., Sodr e, Jr., L., & Balkowski, C. 2004, *ApJ*, 605, L17  
 Moles, M., Sulentic, J. W., & Márquez, I. 1997, *ApJ*, 485, L69  
 Mould, J. R., Huchra, J. P., Freedman, W. L., et al. 2000, *ApJ*, 529, 786  
 O'Donnell, J. E. 1994, *ApJ*, 422, 158  
 Ohya, Y., Nishiura, S., Murayama, T., & Taniguchi, Y. 1998, *ApJ*, 492, L25  
 Osterbrock, D. E. 1989, *Astrophysics of gaseous nebulae and active galactic nuclei*  
 Pagel, B. E. J., Edmunds, M. G., Blackwell, D. E., Chun, M. S., & Smith, G. 1979, *MNRAS*, 189, 95  
 Pérez, F. & Granger, B. E. 2007, *Computing in Science and Engineering*, 9, 21  
 Pérez-Montero, E. 2014, *MNRAS*, 441, 2663  
 Pérez-Montero, E. & Contini, T. 2009, *MNRAS*, 398, 949  
 Pilyugin, L. S. & Grebel, E. K. 2016, *MNRAS*, 457, 3678  
 Renaud, F., Appleton, P. N., & Xu, C. K. 2010, *ApJ*, 724, 80  
 Robitaille, T. & Bressert, E. 2012, *APLpy: Astronomical Plotting Library in Python*, *Astrophysics Source Code Library*  
 Rodríguez-Baras, M., Díaz, A. I., Rosales-Ortega, F. F., & Sánchez, S. F. 2018, *A&A*, 609, A102  
 Rodríguez-Baras, M., Rosales-Ortega, F. F., Díaz, A. I., Sánchez, S. F., & Pasquali, A. 2014, *MNRAS*, 442, 495  
 Sánchez, S. F., Rosales-Ortega, F. F., Iglesias-Páramo, J., et al. 2014, *A&A*, 563, A49  
 Schlegel, D. J., Finkbeiner, D. P., & Davis, M. 1998, *ApJ*, 500, 525  
 Stephan, M. 1877, *MNRAS*, 37, 334  
 Storey, P. J. & Hummer, D. G. 1995, *MNRAS*, 272, 41  
 Sulentic, J. W., Rosado, M., Dultzin-Hacyan, D., et al. 2001, *AJ*, 122, 2993  
 Tsamis, Y. G., Walsh, J. R., Vilchez, J. M., & Péquignot, D. 2011, *MNRAS*, 412, 1367  
 Van Der Walt, S., Colbert, S. C., & Varoquaux, G. 2011, *ArXiv e-prints*  
 van Zee, L. & Haynes, M. P. 2006, *ApJ*, 636, 214  
 Verdes-Montenegro, L., Yun, M. S., Williams, B. A., et al. 2001, *A&A*, 377, 812  
 Williams, B. A., Yun, M. S., & Verdes-Montenegro, L. 2002, *AJ*, 123, 2417  
 Xu, C., Sulentic, J. W., & Tuffs, R. 1999, *ApJ*, 512, 178  
 Xu, C. K., Iglesias-Páramo, J., Burgarella, D., et al. 2005, *ApJ*, 619, L95

## Appendix A: The Stephan's Quintet, zone by zone

- YTT: The young tidal tail (YTT) is located between the AGN galaxy NGC 7319 and the older intruder, NGC7320c. YTT is composed of 17 H $\alpha$  emission regions. We divided the area into two sub-zones: north (YTTN) and South (YTTS). YTTN corresponds to the trace of a possible filament that points towards the rest of YTT, as can be seen in the upper left panel of Fig. 1 in [Duc et al. \(2018\)](#). YTTN consists of 6 H $\alpha$  emission regions and YTTS of 11. The average radial velocity in YTT is  $\sim 6620 \text{ km s}^{-1}$ . On average, the  $A_v$  extinction in YTTS is higher than in YTTN (2.3 and 0.7, respectively). Of the 17 initial regions, 12 are HII regions, 1 is composite, and the rest are not found in the BPT diagram.<sup>11</sup> Except for region 15 (SQB) the remaining regions have a relatively low  $\log(\text{SFR}/M_{\odot} \text{ yr}^{-1})$  ( $< -1.2$ ) reaching values up to  $\sim -2.8$  (reg 12). In SQB, the  $\log(\text{SFR}/M_{\odot} \text{ yr}^{-1})$  is  $\sim -0.7$ . The average metallicity in YTT is  $\sim 8.52$  ( $\sim 70\%$  solar value). According to [Mendes de Oliveira et al. \(2004\)](#), the average metallicity using the N2 calibrator is  $\sim 8.58$  (we derive  $\sim 8.6$  when using this calibrator). Also, we found a solar value for N/O in YTT, on average.
- NGC 7319:
  - North lobe: Zone located at North of the active galactic nuclei NGC 7319 and composed of 7 H $\alpha$  emission regions, of which only two are HII regions. The average radial velocity is  $\sim 6780 \text{ km s}^{-1}$ . Although there is absence of molecular gas, the average  $A_v$  extinction is high ( $\sim 3$  mag), where the minimum is  $\sim 1.2$  and the maximum is 4.2. The average  $\log(\text{SFR}/M_{\odot} \text{ yr}^{-1})$  in both HII regions is  $-1.64$  and the metallicity is solar. N/O is higher than solar value ( $\sim -0.65$ ).
  - NGC 7319 arm: We detected 3 H $\alpha$  emission regions in this zone. The radial velocity covers a range from 6600 to 6715  $\text{ km s}^{-1}$ . The average  $A_v$  extinction is 0.9 mag. We did not find any region in the BPT diagram.
  - NGC 7319 N: In NGC 7319 nuclei we found 3 H $\alpha$  emission regions with radial velocities between 6690 and 6355  $\text{ km s}^{-1}$ . As expected, all regions are AGN-like in the BPT diagram. The average  $A_v$  extinction is  $\sim 1.5$  mag, showing a double core (1.5 and 2.5 mag) that would imply we detected an outflow.
- NSQA: North of SQA, consisting of 13 H $\alpha$  emission regions, 11 of which are HII regions. The average radial velocity is  $\sim 5970 \text{ km s}^{-1}$ . The average  $A_v$  extinction is  $\sim 1$  mag. The mean  $\log(\text{SFR}/M_{\odot} \text{ yr}^{-1})$  is  $-1.5$ , where the maximum is placed in the region 129 ( $-1.22$ ) and the minimum in the region 147 ( $-2.1$ ). On average, the regions show a metallicity value of  $\sim 8.6$  and a N/O of  $\sim -0.8$ .
- SDR: SDR is located at South of NI and is composed of 13 H $\alpha$  regions, of which 9 appear in the BPT diagram, being all HII regions. The average radial velocity is  $\sim 5720 \text{ km s}^{-1}$ , with a range of radial velocities from  $\sim 5620$  to  $\sim 5870 \text{ km s}^{-1}$ . We found an average  $A_v$  value lower than  $\sim 0.65$  mag. The mean  $\log(\text{SFR}/M_{\odot} \text{ yr}^{-1})$  is  $\sim -2$ , the metallicity is  $\sim 65\%$  of the solar value ( $\sim 8.5$ ) and the N/O is  $-0.9$ .
- SQ-A: Divided into two zones with a radial velocity  $\sim 6670 \text{ km s}^{-1}$ . Both are HII regions. The  $A_v$  extinction in both regions is  $\sim 2.3$  mag. In paper I, Fig. 6 (upper panel) we can see two well differentiated zones. Region 122 (North) has

a higher  $\log(\text{SFR}/M_{\odot} \text{ yr}^{-1})$  than region 121 (South). Region 122 has a  $\log(\text{SFR}/M_{\odot} \text{ yr}^{-1}) = -0.13$ , while region 121 has  $-0.85$ . The sum of both  $\log(\text{SFR}/M_{\odot} \text{ yr}^{-1})$  is  $-0.06$ . Region 122 is traditionally associated with starburst A (e.g. the placement of the spectroscopic slit of SQA by [Konstantopoulos et al. 2014](#)). O/H and N/O are similar for both regions,  $\sim 8.45$  y  $\sim -1$ , respectively.

- Hs: The high velocity strands (Hs) encompass sub-zones H1 and H2. The H1 strand is composed of 4 H $\alpha$  regions and H2 has 5. From paper I it can be seen that the H2 strand connects SQA with the high radial velocity region detected in paper I for SQ (reg 111.  $v \sim 7000 \text{ km s}^{-1}$ ). The H1 strand links region 111 with the shocked strands (Shs). Two of the H $\alpha$  emission regions are HII regions (one per filament) while the other one is composite. Both  $\log(\text{SFR}/M_{\odot} \text{ yr}^{-1})$  are relatively low ( $\sim -1.7$  and  $\sim -3.2$ ). The metallicity is  $\sim 8.6$  and the N/O is lower than the solar value.
- Ls: The Ls strands (low velocity strands) encompass sub-zones L1, L2, L3, and L4. The L1 strand is composed of 23 H $\alpha$  regions, L2 of 4, L3 of 3, and the L4 strand of 3. The average radial velocity in this zone is  $\sim 6000 \text{ km s}^{-1}$  and its average  $A_v$  extinction is  $\sim 0.9$  mag. We did not find any region from the L3 strand in the BPT diagram. Conversely, strands L1, L2, and L4 have 16, 2, and 3 regions in the BPT diagram. All regions detected in L2 and L4 are HII regions, while in the L1 strand only four are HII region, and the rest are consistent with fast shock ionisation without precursor for solar metallicity and low density with velocities between 175 and 300  $\text{ km s}^{-1}$  using the models from [Allen et al. \(2008\)](#). The average  $\log(\text{SFR}/M_{\odot} \text{ yr}^{-1})$  for Ls is  $\sim -2.15$  and the metallicity is  $\sim 80\%$  of the solar value ( $\sim 8.6$ ), while the N/O is solar.
- SSQA: SSQA is composed of 9 H $\alpha$  emission regions with an average radial velocity of  $\sim 6020 \text{ km s}^{-1}$ . The average  $A_v$  extinction is  $\sim 1.3$  mag. Two regions are SF and five are composite. Both regions present a metallicity value of  $\sim 8.6$  and a N/O of  $\sim -0.9$ .
- NW: NW is a tidal tail located at North of NSQA which seems to link with NSQA ([Renaud et al. 2010](#); [Duc et al. 2018](#)). NW is composed of 5 H $\alpha$  emission regions with an average radial velocity of 6030  $\text{ km s}^{-1}$ . The  $A_v$  extinction is low ( $\sim 0.4$  mag). Two H $\alpha$  emission region are HII regions. The average  $\log(\text{SFR}/M_{\odot} \text{ yr}^{-1})$  is low ( $-2.3$ ). Additionally, the metallicity in these region is half-solar (8.45) and its N/O is lower than the solar value ( $\sim -1$ ).
- Shs: The shock strands (Shs) encompass the strands Sh1, Sh2, Sh3, and Sh4. Shs connect the Hs and Ls zones. The Sh1 and Sh4 strands have 9 regions each, while the Sh2 and Sh3 strands have 10 and 22 regions, respectively. The radial velocities are between 6000  $\text{ km s}^{-1}$  and 6850  $\text{ km s}^{-1}$ .  $A_v$  extinction mean values in Sh1, Sh2, Sh3, and Sh4 are 1.2, 0.8, 1.2, 0.8 mag, respectively. Fourteen regions in Shs are found in the BPT diagram, being all HII regions. The mean  $\log(\text{SFR}/M_{\odot} \text{ yr}^{-1})$  is lower than  $\sim -1.9$ . The metallicity in the different strands varies slightly. The strands Sh1 and Sh4 have a mean metallicity of  $\sim 8.65$ , even though region 104 has a half-solar metallicity value. The average metallicity in strands Sh2 and Sh3 is 8.45, where the minimum metallicity value derived for the stand Sh2 has a half-solar value ( $\sim 8.4$ ) while the minimum in the strand Sh3 is almost a quarter of the solar value ( $\sim 8$ , region 59). The mean N/O is lower than the solar value. In the strands Sh1, Sh2, and Sh4 the average  $\log(\text{N/O})$  is  $\sim -1$ , while in the strand Sh3 it is  $\sim -1.3$ . In Sh3, the lowest N/O derived is  $\sim -1.6$  (region 59).
- NG: NG is a new SQ M82-like dwarf galaxy. NG has an average radial velocity of  $\sim 6250 \text{ km s}^{-1}$  and presents a ra-

<sup>11</sup> Only the H $\alpha$  emission regions spectra showing the four BPT emission line (i.e. [OIII] $\lambda 5007$ , H $\beta$ , [NII] $\lambda 6584$ , and H $\alpha$ ) fluxes with SNR  $\geq 3$  have been spectroscopically classified. This applies to all the other zones describe in App. A.

dial velocity gradient of  $+60 \text{ km s}^{-1}$ . The  $A_v$  extinction is 3.5 mag. NG is a star-forming galaxy according to the BPT diagram. Its  $\log(\text{SFR}/M_{\odot} \text{ yr}^{-1})$  is -1.05. Both metallicity and N/O in this galaxy are slightly lower than the half-solar value (8.27 and -1.31, respectively).

- Bridge: As discussed in paper I, the emission detected in the bridge presents a low  $\text{H}\alpha$  surface emission. Two  $\text{H}\alpha$  emission regions were detected in this zone with a mean radial velocity of  $\sim 6420 \text{ km s}^{-1}$  and a mean  $A_v$  extinction of  $\sim 1.8$  mag. One region is composite and the other one is an HII region. The  $\log(\text{SFR}/M_{\odot} \text{ yr}^{-1})$  in the detected HII region (region 35) is -1.6, with a metallicity which is almost solar ( $\sim 8.7$ ) and N/O -1.
- NI: In order to study each zone in more detail, we divided the new intruder (NI) into 5 sub-zones. We found 29  $\text{H}\alpha$  emission regions in NI. The radial velocity covers the range between  $\sim 5600$  and  $\sim 5850 \text{ km s}^{-1}$ . The average  $A_v$  extinction is lower than 1.2 mag. The regions contaminated by the LSSR in NI (regions from NI1) are the regions with the highest  $A_v$  values. Twenty-five regions are found in the BPT diagram. Except for one region in zone NI4, the other are HII regions. The  $\log(\text{SFR}/M_{\odot} \text{ yr}^{-1})$  covers a range from  $\sim -0.9$  (region 117) to  $\sim -2.5$  (region 149), the average value being  $\sim -1.7$ . The mean metallicity is  $\sim 8.6$  and the average N/O has a solar value.

## Appendix B: Oxygen abundance using the R calibrator

In Fig. B.1 we show the oxygen abundance maps for LV (upper panel) and HV (lower panel) sub-samples using the R calibrator from Pilyugin & Grebel (2016). See Sect. 2.5 for more detail.

## Appendix C: Additional table

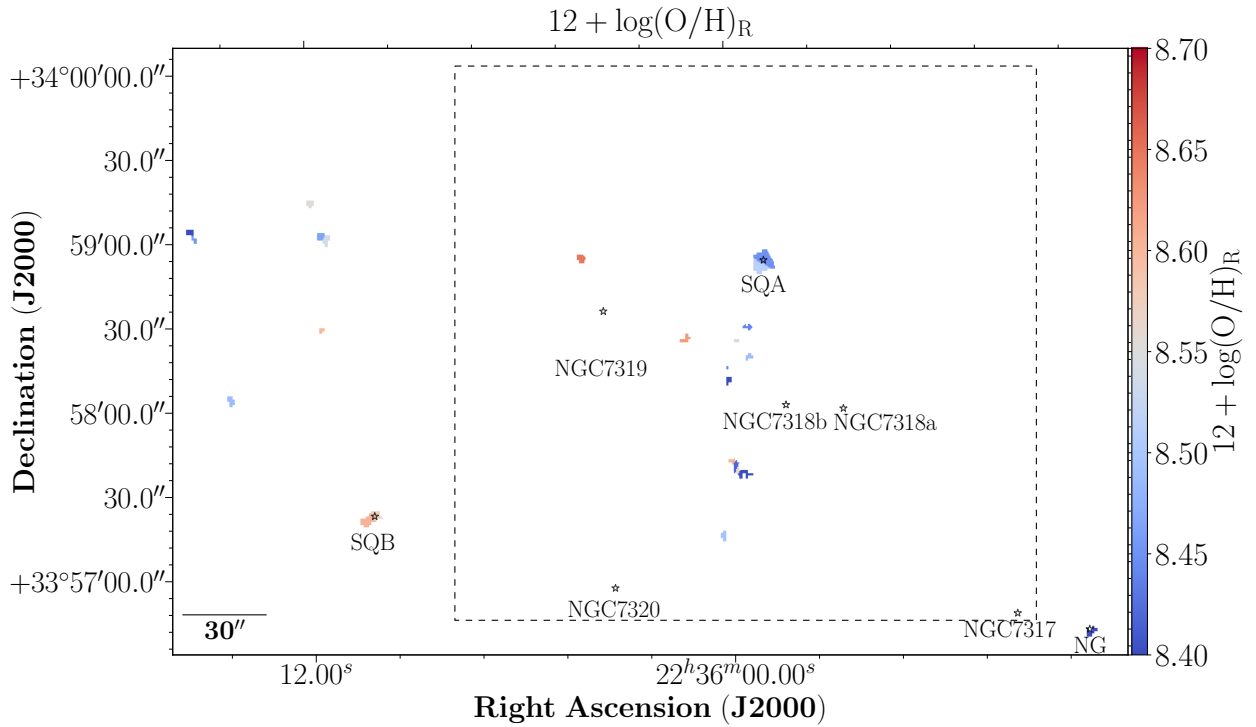
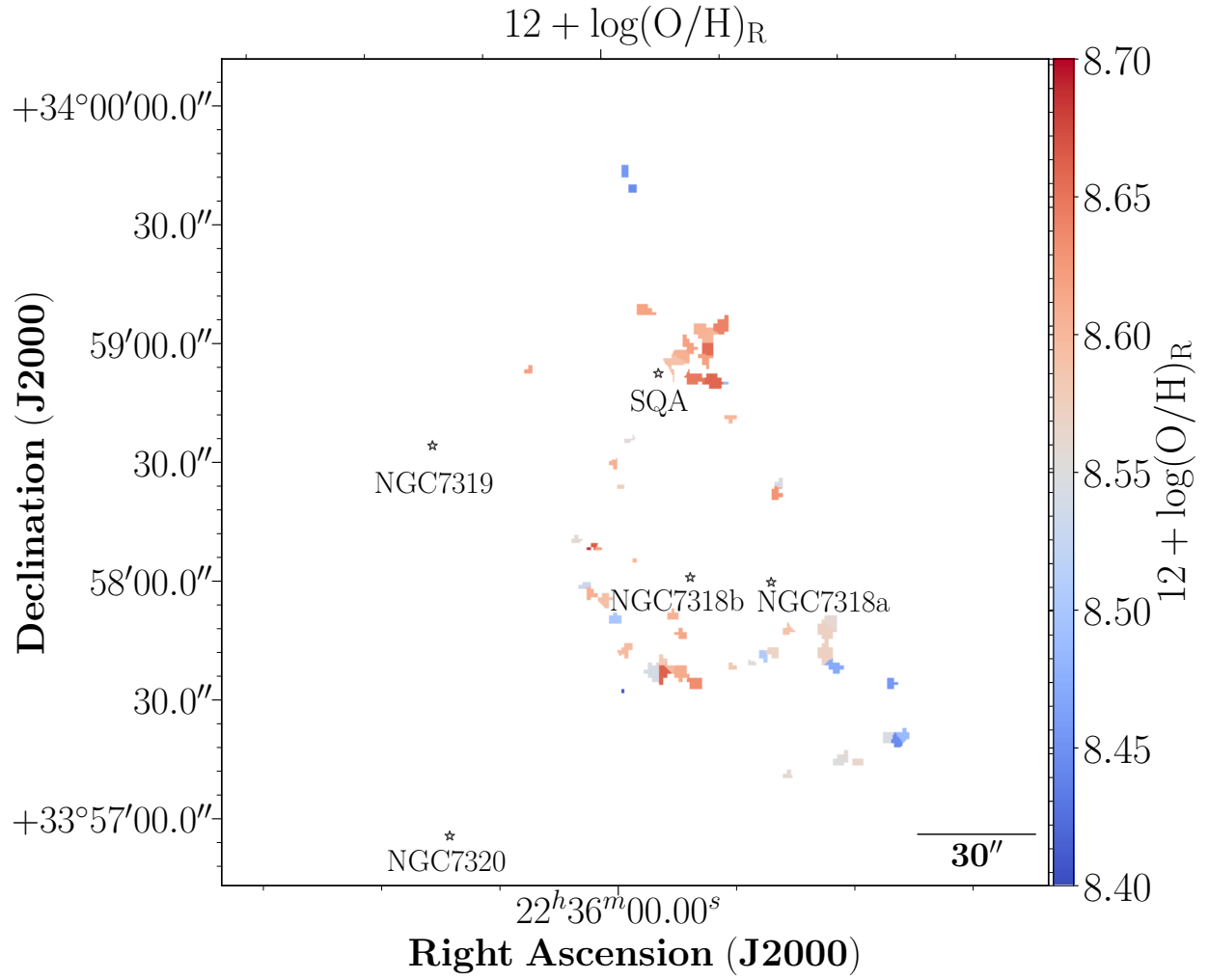


**Fig. B.1.** SQ spatial map colour coded according to their  $12 + \log(\text{O}/\text{H})$  derived using the R calibrator from Pilyugin & Grebel (2016) calibrator for LV sub-sample (upper left panel) and HV sub-sample (upper right panel).

**Table C.1.** Reddening corrected line fluxes relative to  $H\beta = 100$ .

(1) Region ID	(2) [OII] $\lambda$ 3727	(3) [OIII] $\lambda$ 5007	(4) H $\alpha$	(5) [NII] $\lambda$ 6584	(6) [SII] $\lambda$ 6716	(7) [SII] $\lambda$ 6731	(8) A <sub>v</sub>	(9) Vel (mag)	(10) Zone	(11) Subzone
1*	–	–	–	–	–	–	–	–	NGC7320c	NGC7320c
2	341.8±87.3	188.0±31.8	286.0±43.3	30.5±10.1	–	–	1.4	1	YTT	YTT
3	486.2±186.5	184.6±65.7	286.0±91.4	75.3±19.7	–	–	2.5	1	YTT	YTT
4	236.0±66.5	165.4±22.8	286.0±33.0	62.7±6.1	–	–	1.8	1	YTT	YTT
5	–	80.9±35.6	249.2±79.5	182.6±40.1	–	–	0.0	1	YTT	YTT
6	–	298.9±107.8	286.0±99.4	51.4±14.8	–	–	2.9	1	YTT	YTT
7	–	–	276.0±88.2	–	–	–	0.0	1	YTT	YTT
8	–	75.7±26.5	286.0±63.6	70.9±13.8	–	–	2.9	1	YTT	YTT
9	191.4±53.4	152.0±24.7	286.0±39.2	75.6±9.2	–	–	0.7	1	YTT	YTT
10	177.4±30.0	244.2±19.8	286.0±21.3	47.9±4.2	–	–	1.3	1	YTT	YTT
11	143.7±44.1	136.3±29.2	286.0±51.7	85.5±15.1	–	–	0.4	1	YTT	YTT
12	–	62.2±24.4	286.0±67.4	76.8±20.2	–	–	0.4	1	YTT	YTT
13	153.6±42.0	240.5±24.7	286.0±26.4	62.8±4.2	–	–	2.3	1	YTT	YTT
14	193.8±60.2	66.6±13.9	286.0±35.6	102.7±9.6	–	–	3.1	1	YTT	YTT
15	123.7±26.2	155.4±18.8	286.0±28.7	71.5±5.5	–	–	3.2	1	YTT	YTT
16	–	–	286.0±97.0	114.4±19.9	–	–	1.3	1	YTT	YTT
17	–	–	286.0±61.5	128.7±16.8	–	–	2.3	1	YTT	YTT
18	–	–	286.0±77.3	117.9±26.3	–	–	1.4	1	NGC7319	NGC7319 Arm
19	167.0±69.6	–	286.0±83.8	111.4±15.8	–	–	1.2	1	YTT	YTT
20	–	–	286.0±61.9	106.8±13.6	–	–	4.2	1	NGC7319	North lobe
21	–	–	286.0±71.2	115.3±13.2	–	–	3.0	1	NGC7319	North lobe
22 <sup>†</sup>	–	–	286.0±117.6	163.7±66.4	–	–	1.9	1	NGC7319	NGC7319 Arm
23	–	–	286.0±78.6	105.8±22.0	–	–	3.3	1	NGC7319	North lobe
24	141.6±39.5	56.1±19.7	286.0±62.0	115.8±18.4	–	–	2.0	1	NGC7319	North lobe
25	–	48.9±17.4	286.0±58.2	135.3±21.1	–	–	1.7	1	NGC7319	North lobe
26	507.4±151.0	951.4±280.0	286.0±85.6	385.0±36.0	–	–	2.5	1	NGC7319	NGC7319 Nucl.
27	278.0±95.3	793.7±268.3	286.0±99.5	289.1±40.7	–	–	1.5	1	NGC7319	NGC7319 Nucl.
28	–	–	286.0±85.9	100.4±25.3	–	–	0.4	1	NGC7319	NGC7319 Arm
29	259.4±110.7	756.2±257.4	286.0±103.7	252.5±55.6	–	–	0.6	1	NGC7319	NGC7319 Nucl.
30	–	119.5±53.0	286.0±102.5	170.5±39.8	–	–	3.1	1	NGC7319	North lobe
31 <sup>†</sup>	172.9±86.6	298.2±116.1	286.0±111.8	–	–	–	0.3	0	Ls	L1
32	–	–	286.0±90.3	133.2±40.5	–	–	1.2	1	NGC7319	North lobe
33	156.5±46.4	104.6±23.5	256.4±51.1	97.7±25.4	–	–	0.0	0	Ls	L2
34	–	–	283.1±70.2	–	–	–	0.0	1	NW	NW
35	491.4±129.1	65.7±20.3	286.0±62.1	144.7±31.9	–	–	1.9	1	Bridge	Bridge
36	–	165.4±57.4	265.2±94.6	–	–	–	0.0	0	Ls	L2
37	192.5±47.4	154.4±30.8	274.5±52.2	–	–	–	0.0	0	NW	NW
38	–	168.5±56.4	286.0±93.7	–	–	–	1.0	0	NIs	NI1
39	187.5±53.7	188.8±40.7	286.0±57.8	73.0±18.5	–	–	1.0	0	Ls	L1
40	541.6±149.6	141.0±29.5	286.0±56.0	183.3±31.0	–	–	1.6	1	Bridge	Bridge
41	–	197.1±75.1	286.0±98.9	–	–	–	0.7	0	Ls	L2
42	259.4±68.6	107.9±24.8	286.0±51.2	80.5±16.2	40.8±13.0	–	1.2	0	NIs	NI1
43	–	139.6±56.8	286.0±98.4	129.8±32.4	–	–	1.3	0	Ls	L1
44	–	–	286.0±89.5	115.8±31.2	–	–	1.2	0	Ls	L1
45	428.9±140.6	95.3±36.8	286.0±83.3	125.4±27.5	104.1±25.7	–	1.4	0	NIs	NI1
46	–	58.4±20.3	286.0±55.4	69.4±16.1	61.1±17.1	–	1.6	0	NIs	NI1
47	121.7±42.9	53.3±19.7	249.2±61.0	135.9±37.1	–	–	0.0	0	Ls	L1
48	282.9±115.8	91.3±34.1	286.0±85.0	136.2±42.3	–	–	1.8	0	Ls	L1
49	361.7±101.6	–	286.0±71.9	–	121.3±33.8	–	1.8	0	NIs	NI1
50	567.7±193.0	88.6±33.2	286.0±81.4	141.4±36.0	–	–	1.1	0	Ls	L1
51 <sup>a</sup>	323.2±126.3	–	286.0±85.0	–	–	–	1.6	0	Shs	Sh1
51 <sup>b</sup>	507.3±159.4	79.3±27.4	286.0±80.6	99.1±33.5	–	–	1.6	1	Shs	Sh1
52	207.2±54.6	63.8±18.3	286.0±51.6	101.3±11.6	69.9±10.1	–	1.4	0	NIs	NI1
53	441.0±180.1	112.0±45.1	220.0±77.2	221.0±63.0	153.3±54.2	–	0.0	0	Ls	L1
54	327.7±113.8	98.9±34.3	286.0±80.8	192.1±43.9	–	–	1.0	0	Ls	L1
55 <sup>†</sup>	275.4±129.0	–	286.0±102.8	199.4±76.9	–	–	0.6	0	Ls	L1
56 <sup>v</sup>	–	–	218.9±73.6	–	–	–	0.1	1	Shs	Sh3
57	–	–	281.5±107.0	516.7±170.7	–	–	0.0	0	Ls	L1
58 <sup>a</sup>	488.9±144.3	146.5±38.4	286.0±78.6	337.9±75.0	181.1±44.7	–	1.1	0	Ls	L1
58 <sup>b</sup>	–	133.2±75.3	286.0±152.5	88.2±37.1	–	–	1.9	1	Shs	Sh3

Notes. Continued.

(1)	(2)	(3)	(4)	(5)	(6)	(7)	(8)	(9)	(10)	(11)
Region ID	[OII] $\lambda$ 3727	[OIII] $\lambda$ 5007	H $\alpha$	[NII] $\lambda$ 6584	[SII] $\lambda$ 6716	[SII] $\lambda$ 6731	A $_v$	Vel (mag)	Zone	Subzone
59 <sup>a</sup>	155.5 $\pm$ 34.4	69.6 $\pm$ 15.4	253.1 $\pm$ 48.9	208.1 $\pm$ 48.9	133.3 $\pm$ 30.7	–	0.0	0	Ls	L1
59 <sup>b</sup>	1009.2 $\pm$ 250.4	67.9 $\pm$ 26.3	286.0 $\pm$ 86.9	39.1 $\pm$ 14.3	–	–	2.3	1	Shs	Sh3
60 <sup>a</sup>	211.9 $\pm$ 77.3	49.5 $\pm$ 17.1	270.8 $\pm$ 57.5	292.6 $\pm$ 78.6	–	–	0.0	0	Ls	L1
60 <sup>b</sup>	997.2 $\pm$ 355.3	145.4 $\pm$ 46.8	286.0 $\pm$ 91.0	99.6 $\pm$ 26.9	–	–	3.0	1	Shs	Sh3
61	183.9 $\pm$ 67.6	–	286.0 $\pm$ 91.5	234.0 $\pm$ 58.7	129.6 $\pm$ 45.4	–	0.3	0	SSQA	SSQA
62 <sup>v</sup>	194.9 $\pm$ 51.6	–	265.3 $\pm$ 48.1	74.1 $\pm$ 21.1	–	–	0.0	1	Shs	Sh1
63	256.8 $\pm$ 98.8	–	286.0 $\pm$ 83.1	130.6 $\pm$ 48.4	–	–	1.0	1	Shs	Sh1
64	171.3 $\pm$ 41.6	37.7 $\pm$ 13.6	286.0 $\pm$ 50.3	104.4 $\pm$ 35.4	–	–	0.4	1	Shs	Sh2
65	327.9 $\pm$ 132.4	82.2 $\pm$ 32.4	286.0 $\pm$ 77.9	83.4 $\pm$ 13.7	47.7 $\pm$ 12.8	–	2.4	0	NIs	NI1
66 <sup>a</sup>	728.8 $\pm$ 301.5	135.1 $\pm$ 41.8	286.0 $\pm$ 80.2	260.7 $\pm$ 55.8	85.1 $\pm$ 22.0	–	2.9	0	Ls	L1
66 <sup>b</sup>	675.8 $\pm$ 312.9	–	286.0 $\pm$ 104.6	–	–	–	1.3	1	Shs	Sh3
67	–	70.8 $\pm$ 26.2	286.0 $\pm$ 75.6	209.0 $\pm$ 44.7	122.2 $\pm$ 35.2	–	2.1	0	Ls	L1
68 <sup>a</sup>	305.2 $\pm$ 82.8	66.8 $\pm$ 22.2	286.0 $\pm$ 60.8	246.8 $\pm$ 48.2	85.6 $\pm$ 20.2	–	1.1	0	Ls	L1
68 <sup>b</sup>	416.7 $\pm$ 138.6	–	286.0 $\pm$ 106.9	–	–	–	0.6	1	Shs	Sh3
69 <sup>a</sup>	–	93.5 $\pm$ 37.5	286.0 $\pm$ 97.8	168.9 $\pm$ 54.3	152.6 $\pm$ 49.5	–	0.5	0	Ls	L1
69 <sup>b†</sup>	318.9 $\pm$ 147.6	–	273.6 $\pm$ 107.6	126.9 $\pm$ 58.1	–	–	0.0	1	Shs	Sh4
70	330.5 $\pm$ 102.1	56.1 $\pm$ 20.8	286.0 $\pm$ 56.0	125.6 $\pm$ 16.6	82.1 $\pm$ 15.7	–	1.9	0	SSQA	SSQA
71	145.2 $\pm$ 50.9	45.2 $\pm$ 15.3	264.0 $\pm$ 48.9	209.7 $\pm$ 36.4	90.4 $\pm$ 26.9	–	0.0	0	SSQA	SSQA
72	166.5 $\pm$ 64.0	78.4 $\pm$ 33.7	259.0 $\pm$ 82.2	–	–	–	0.0	1	Shs	Sh1
73	–	44.5 $\pm$ 15.7	280.0 $\pm$ 53.5	–	–	–	0.0	1	Shs	Sh1
74	280.5 $\pm$ 67.1	33.3 $\pm$ 12.3	286.0 $\pm$ 51.0	66.8 $\pm$ 20.5	–	–	1.1	1	Shs	Sh2
75	159.2 $\pm$ 47.1	63.8 $\pm$ 19.7	286.0 $\pm$ 50.9	94.3 $\pm$ 24.0	93.3 $\pm$ 24.6	–	0.8	0	NIs	NI1
76 <sup>a</sup>	369.7 $\pm$ 98.8	56.8 $\pm$ 15.9	286.0 $\pm$ 54.8	118.2 $\pm$ 30.2	83.0 $\pm$ 22.6	–	1.1	0	Shs	Sh4
76 <sup>b</sup>	416.1 $\pm$ 138.5	65.1 $\pm$ 23.3	286.0 $\pm$ 76.4	114.3 $\pm$ 38.9	–	–	0.8	1	Shs	Sh4
77	204.6 $\pm$ 62.2	64.0 $\pm$ 19.4	286.0 $\pm$ 61.2	86.8 $\pm$ 29.0	–	–	0.7	1	Shs	Sh2
78	370.1 $\pm$ 121.6	78.9 $\pm$ 26.7	286.0 $\pm$ 76.8	42.8 $\pm$ 14.5	82.2 $\pm$ 18.7	–	1.3	0	Shs	Sh1
79 <sup>a</sup>	496.8 $\pm$ 184.0	–	286.0 $\pm$ 103.0	135.5 $\pm$ 49.2	–	–	1.3	0	Shs	Sh3
79 <sup>b</sup>	703.9 $\pm$ 230.4	112.2 $\pm$ 34.7	286.0 $\pm$ 74.0	–	–	–	2.4	1	Shs	Sh3
80 <sup>a</sup>	–	–	286.0 $\pm$ 74.6	152.3 $\pm$ 47.2	–	–	0.2	0	Shs	Sh4
80 <sup>b v</sup>	–	–	147.4 $\pm$ 48.2	–	–	–	0.0	1	Shs	Sh4
81 <sup>a</sup>	–	179.3 $\pm$ 60.2	286.0 $\pm$ 95.6	123.1 $\pm$ 43.2	–	–	1.5	0	Ls	L1
81 <sup>b</sup>	–	61.5 $\pm$ 24.6	249.2 $\pm$ 73.1	–	–	–	0.0	1	Shs	Sh4
82	244.7 $\pm$ 59.4	159.3 $\pm$ 27.0	286.0 $\pm$ 42.2	57.1 $\pm$ 10.9	42.5 $\pm$ 11.4	–	0.6	0	NW	NW
83 <sup>a</sup>	570.6 $\pm$ 243.3	–	286.0 $\pm$ 110.3	98.8 $\pm$ 36.2	–	–	2.5	0	Shs	Sh2
83 <sup>b</sup>	385.5 $\pm$ 88.1	81.4 $\pm$ 20.1	286.0 $\pm$ 62.3	58.3 $\pm$ 17.1	–	–	1.3	1	Shs	Sh2
84	452.9 $\pm$ 138.0	–	286.0 $\pm$ 66.6	–	–	–	1.4	1	Shs	Sh3
85	–	–	286.0 $\pm$ 84.7	82.7 $\pm$ 29.2	–	–	0.4	1	Shs	Sh3
86 <sup>a</sup>	590.7 $\pm$ 271.9	133.8 $\pm$ 53.5	286.0 $\pm$ 106.7	304.7 $\pm$ 74.8	110.7 $\pm$ 32.5	–	2.7	0	Ls	L1
86 <sup>b†</sup>	337.3 $\pm$ 152.9	–	260.2 $\pm$ 117.4	157.2 $\pm$ 76.1	–	–	0.0	1	Shs	Sh3
87 <sup>a</sup>	376.4 $\pm$ 125.2	–	286.0 $\pm$ 90.3	–	–	–	1.4	0	Shs	Sh3
87 <sup>b†</sup>	–	67.7 $\pm$ 41.0	286.0 $\pm$ 118.5	–	–	–	3.1	1	Shs	Sh3
88	–	–	286.0 $\pm$ 82.0	192.1 $\pm$ 45.9	–	–	1.7	1	Ls	L1
89 <sup>a</sup>	265.2 $\pm$ 105.5	–	286.0 $\pm$ 85.1	–	–	–	0.5	0	Shs	Sh4
89 <sup>b†</sup>	–	–	256.9 $\pm$ 101.7	128.2 $\pm$ 58.7	–	–	0.0	1	Shs	Sh4
90	333.8 $\pm$ 106.6	110.4 $\pm$ 29.3	286.0 $\pm$ 59.5	139.5 $\pm$ 18.5	57.8 $\pm$ 15.5	–	1.6	0	SSQA	SSQA
91	307.3 $\pm$ 95.5	65.7 $\pm$ 24.5	286.0 $\pm$ 67.5	100.8 $\pm$ 26.0	–	–	1.3	0	SSQA	SSQA
92	838.2 $\pm$ 364.9	397.8 $\pm$ 130.9	286.0 $\pm$ 93.5	93.4 $\pm$ 22.6	–	–	1.5	0	SSQA	SSQA
93 <sup>v</sup>	–	–	218.2 $\pm$ 69.5	–	180.5 $\pm$ 54.2	–	0.0	0	Shs	Sh1
94 <sup>a</sup>	–	–	286.0 $\pm$ 101.7	113.3 $\pm$ 31.6	–	–	2.0	0	NIs	NI1
94 <sup>b</sup>	–	–	231.7 $\pm$ 70.7	142.8 $\pm$ 50.7	–	–	0.0	1	Shs	Sh2
95 <sup>a†</sup>	–	–	237.0 $\pm$ 135.6	212.2 $\pm$ 126.6	–	–	0.0	0	Shs	Sh2
95 <sup>b</sup>	203.1 $\pm$ 69.4	–	271.6 $\pm$ 64.5	–	–	–	0.0	1	Shs	Sh2
96	335.4 $\pm$ 104.4	61.5 $\pm$ 19.5	286.0 $\pm$ 58.7	72.9 $\pm$ 19.5	–	–	1.8	1	Hs	H2
97	126.2 $\pm$ 32.1	377.8 $\pm$ 62.5	286.0 $\pm$ 47.9	34.9 $\pm$ 11.9	–	–	0.4	0	NW	NW
98	456.7 $\pm$ 142.8	78.3 $\pm$ 22.6	286.0 $\pm$ 57.1	212.3 $\pm$ 28.8	86.2 $\pm$ 20.7	–	2.0	0	SSQA	SSQA
99	454.8 $\pm$ 181.5	99.6 $\pm$ 32.1	286.0 $\pm$ 84.4	–	–	–	1.3	1	Shs	Sh1
100 <sup>a</sup>	–	–	232.8 $\pm$ 83.6	149.3 $\pm$ 59.3	–	–	0.0	0	Shs	Sh3
100 <sup>b</sup>	–	–	258.0 $\pm$ 92.3	–	–	–	0.0	1	Shs	Sh2
101	272.7 $\pm$ 91.1	–	286.0 $\pm$ 89.7	183.5 $\pm$ 71.8	–	–	0.5	1	Shs	Sh3
102 <sup>a</sup>	424.2 $\pm$ 170.3	110.2 $\pm$ 37.3	286.0 $\pm$ 89.1	120.1 $\pm$ 40.1	61.3 $\pm$ 23.8	–	1.3	0	Shs	Sh3
102 <sup>b</sup>	–	–	218.3 $\pm$ 97.1	–	–	–	0.0	1	Shs	Sh3

(1)	(2)	(3)	(4)	(5)	(6)	(7)	(8)	(9)	(10)	(11)
Region ID	[OII] $\lambda$ 3727	[OIII] $\lambda$ 5007	H $\alpha$	[NII] $\lambda$ 6584	[SII] $\lambda$ 6716	[SII] $\lambda$ 6731	A <sub>v</sub>	Vel (mag)	Zone	Subzone
103 <sup>a†</sup>	–	112.7±46.0	286.0±103.3	263.3±97.8	–	–	1.9	0	Ls	L1
103 <sup>b∇</sup>	253.1±102.7	–	171.7±58.9	–	–	–	0.0	1	Shs	Sh3
104 <sup>a†</sup>	–	–	228.0±108.8	205.9±102.7	–	–	0.0	0	Shs	Sh4
104 <sup>b</sup>	356.4±101.3	52.9±19.0	286.0±62.0	89.4±23.7	–	–	1.1	1	Shs	Sh4
105	450.5±174.3	–	286.0±88.5	–	–	–	1.9	1	Hs	H2
106	339.7±126.9	–	286.0±83.0	146.4±27.1	–	–	1.3	0	SSQA	SSQA
107	311.8±134.2	–	286.0±111.6	89.5±43.5	–	–	1.3	1	Shs	Sh3
108	335.3±113.8	–	286.0±83.0	–	–	–	1.7	1	Shs	Sh3
109 <sup>∇</sup>	–	71.4±25.9	221.8±71.7	112.9±46.7	–	–	0.0	1	Shs	Sh4
110	311.1±88.3	–	286.0±58.7	89.8±18.3	–	–	0.9	1	Hs	H2
111	244.1±93.4	270.8±85.6	286.0±85.0	–	–	–	1.8	1	Hs	H1
112	228.6±52.2	141.3±26.4	286.0±44.8	102.9±12.5	62.0±12.0	–	0.9	0	Ls	L2
113	–	103.8±38.4	286.0±88.4	103.5±33.7	–	–	1.6	1	Shs	Sh3
114	190.1±60.1	–	258.1±72.6	81.2±30.0	–	–	0.0	1	Shs	Sh3
115	–	–	286.0±66.6	60.6±20.5	–	–	0.6	1	Hs	H2
116	274.9±67.3	–	286.0±54.3	–	–	–	1.0	1	Hs	H2
117	157.6±22.5	149.5±18.5	286.0±28.8	66.7±3.2	26.9±2.5	27.0±2.5	1.0	0	NIIs	NI1
118	425.8±146.5	–	286.0±68.7	40.5±14.3	–	–	1.1	0	NIIs	NI1
119 <sup>∇</sup>	–	–	248.7±80.7	118.0±40.3	–	–	0.0	1	Shs	Sh3
120	190.6±50.0	161.6±29.5	286.0±45.0	133.4±13.5	85.2±12.4	–	0.7	0	SSQA	SSQA
121	357.7±97.4	192.0±37.0	286.0±48.0	79.4±9.5	–	–	2.3	1	SQA	SQA
122	200.7±33.8	204.0±20.3	286.0±24.7	49.0±3.4	–	–	2.3	1	SQA	SQA
123	–	121.3±38.0	242.8±68.2	126.9±42.4	–	–	0.0	1	Hs	H1
124 <sup>†</sup>	305.9±124.8	251.9±94.3	286.0±104.2	–	–	–	1.1	0	NW	NW
125	332.9±124.9	75.1±33.0	286.0±89.8	109.5±29.4	85.7±28.8	–	1.4	0	NIIs	NI2
126	381.3±147.9	224.7±57.5	286.0±67.5	–	–	–	2.8	1	Hs	H1
127	134.3±34.2	83.8±19.1	286.0±46.7	118.0±12.7	92.2±12.4	–	0.3	0	NIIs	NI2
128	362.7±130.0	121.4±45.5	286.0±82.6	111.4±12.9	72.6±12.2	–	1.9	0	NIIs	NI2
129	246.0±54.4	99.9±18.0	286.0±38.0	99.9±7.8	49.8±7.3	–	1.0	0	NSQA	NSQA
130	100.5±30.2	62.5±19.9	286.0±56.6	83.0±9.9	30.6±9.5	–	0.7	0	NIIs	NI3
131	679.4±277.9	262.6±96.9	286.0±99.5	–	–	–	3.0	1	Hs	H1
132	237.7±48.0	126.0±18.6	286.0±33.8	101.8±8.0	63.8±7.7	–	1.4	0	NSQA	NSQA
133	159.7±18.5	177.0±15.6	286.0±21.3	89.4±3.6	40.2±3.4	19.2±3.5	1.0	0	NIIs	NI2
134	202.5±72.4	53.4±20.9	286.0±59.0	111.6±19.3	69.1±18.2	–	1.3	0	NIIs	NI3
135	135.9±55.2	–	286.0±84.6	126.0±21.7	86.6±20.4	–	0.3	0	NSQA	NSQA
136	258.3±79.2	123.7±27.6	286.0±50.4	108.8±11.6	62.0±10.9	–	1.6	0	NSQA	NSQA
137	180.8±49.4	87.9±17.0	286.0±39.1	116.2±10.9	45.8±9.7	–	1.4	0	NSQA	NSQA
138	189.6±44.7	85.9±20.0	286.0±46.5	112.1±8.6	62.5±8.0	36.0±8.0	1.1	0	NIIs	NI2
139	100.5±21.0	124.6±14.2	286.0±26.4	80.3±6.8	52.9±6.8	–	0.3	0	NSQA	NSQA
140	222.9±68.9	90.8±19.7	286.0±46.2	109.4±15.9	44.2±14.3	–	1.5	0	NSQA	NSQA
141	192.7±36.7	120.9±19.6	286.0±36.0	94.6±6.7	53.7±6.4	–	1.0	0	NSQA	NSQA
142	179.4±42.9	104.9±21.8	286.0±44.8	118.0±10.1	75.1±9.5	–	1.1	0	NSQA	NSQA
143	155.9±45.0	81.4±16.6	286.0±39.6	119.9±11.7	76.9±11.0	–	1.0	0	NSQA	NSQA
144 <sup>†</sup>	–	146.3±61.3	286.0±116.3	102.9±51.0	–	–	0.4	0	SDR	SDR
145	–	176.5±60.1	254.5±82.9	–	–	–	0.0	0	NSQA	NSQA
146	161.5±38.8	82.3±14.6	286.0±35.2	111.2±7.3	59.4±6.8	–	1.0	0	NSQA	NSQA
147	814.9±336.9	127.8±48.3	286.0±91.8	105.3±28.4	–	–	2.7	0	NSQA	NSQA
148	270.5±109.7	65.1±25.2	286.0±71.5	112.9±19.9	66.7±19.1	–	1.5	0	Ls	L4
149	300.8±115.5	87.1±29.8	286.0±72.9	105.2±26.6	85.2±26.8	–	0.8	0	NIIs	NI4
150	254.5±76.3	64.4±25.2	286.0±68.8	94.5±20.4	70.4±20.4	–	1.2	0	NIIs	NI4
151	–	94.5±40.6	286.0±90.0	147.8±25.8	89.5±24.8	–	0.6	0	NIIs	NI4
152	175.9±54.9	81.9±28.9	286.0±69.6	64.3±15.5	79.0±17.2	–	1.5	0	NIIs	NI4
153	193.7±48.2	84.3±24.7	286.0±58.6	86.6±11.0	50.2±10.9	–	1.2	0	NIIs	NI4
154	138.0±37.8	114.7±22.0	286.0±42.5	98.2±9.6	41.1±9.0	–	0.7	0	Ls	L4
155	199.1±53.5	215.2±48.7	286.0±57.8	70.6±11.0	–	–	1.3	0	Ls	L4
156	197.6±53.1	121.6±23.9	286.0±49.6	80.3±18.0	–	–	0.2	0	SDR	SDR
157	194.9±55.9	124.3±29.1	286.0±53.7	89.8±12.9	49.3±12.5	–	1.3	0	NIIs	NI4
158	–	81.5±27.1	212.1±65.0	–	134.1±46.7	–	0.0	0	SDR	SDR
159	–	75.2±26.0	286.0±67.7	104.8±16.8	68.1±16.1	–	0.6	0	NIIs	NI4
160	–	185.9±61.3	286.0±87.7	86.8±23.2	–	–	2.2	0	SDR	SDR
161 <sup>a</sup>	–	–	286.0±75.7	48.6±14.0	–	–	2.0	0	Ls	L3
161 <sup>b</sup>	353.9±152.1	–	286.0±112.0	71.8±28.4	–	–	0.5	1	Ls	L3

(1) Region ID	(2) [OII] $\lambda$ 3727	(3) [OIII] $\lambda$ 5007	(4) H $\alpha$	(5) [NII] $\lambda$ 6584	(6) [SII] $\lambda$ 6716	(7) [SII] $\lambda$ 6731	(8) $A_v$	(9) Vel (mag)	(10) Zone	(11) Subzone
162	–	–	221.4 $\pm$ 59.1	103.4 $\pm$ 53.1	–	–	0.0	0	Ls	L3
163	–	154.3 $\pm$ 56.5	286.0 $\pm$ 94.6	–	–	–	0.4	0	SDR	SDR
164	192.5 $\pm$ 26.8	167.8 $\pm$ 19.3	286.0 $\pm$ 27.4	80.0 $\pm$ 4.3	56.5 $\pm$ 4.3	–	0.8	0	NI5	NI5
165	173.3 $\pm$ 24.5	158.9 $\pm$ 19.5	286.0 $\pm$ 29.1	77.9 $\pm$ 4.7	44.2 $\pm$ 4.6	–	0.7	0	NI5	NI5
166	205.5 $\pm$ 37.4	194.9 $\pm$ 26.1	286.0 $\pm$ 33.3	76.8 $\pm$ 6.0	47.8 $\pm$ 6.0	–	1.2	0	NI5	NI5
167	230.3 $\pm$ 47.9	202.9 $\pm$ 31.4	286.0 $\pm$ 38.9	56.8 $\pm$ 6.8	46.4 $\pm$ 7.1	–	1.1	0	NI5	NI5
168	157.4 $\pm$ 37.0	207.4 $\pm$ 32.2	286.0 $\pm$ 39.4	66.9 $\pm$ 7.7	39.1 $\pm$ 7.9	39.0 $\pm$ 11.3	0.0	0	SDR	SDR
169	218.5 $\pm$ 41.8	168.6 $\pm$ 25.8	286.0 $\pm$ 38.7	78.7 $\pm$ 10.8	75.7 $\pm$ 11.5	–	0.7	0	SDR	SDR
170	100.6 $\pm$ 26.3	164.3 $\pm$ 22.6	269.2 $\pm$ 33.4	62.3 $\pm$ 10.6	40.9 $\pm$ 11.0	–	0.0	0	SDR	SDR
171	175.2 $\pm$ 37.2	213.9 $\pm$ 27.4	286.0 $\pm$ 34.0	67.5 $\pm$ 9.0	54.9 $\pm$ 9.5	–	0.2	0	SDR	SDR
172	124.8 $\pm$ 21.9	341.0 $\pm$ 32.3	286.0 $\pm$ 27.0	36.8 $\pm$ 6.7	21.9 $\pm$ 7.2	–	0.6	0	SDR	SDR
173	252.7 $\pm$ 54.6	239.3 $\pm$ 39.9	286.0 $\pm$ 43.0	52.7 $\pm$ 6.7	41.6 $\pm$ 7.1	–	1.0	0	SDR	SDR
174	336.0 $\pm$ 73.4	189.2 $\pm$ 35.7	286.0 $\pm$ 46.1	71.0 $\pm$ 7.7	46.5 $\pm$ 8.2	–	1.3	0	SDR	SDR
175	443.3 $\pm$ 164.6	307.9 $\pm$ 101.0	286.0 $\pm$ 89.5	–	–	–	2.0	0	SDR	SDR
176	600.4 $\pm$ 241.0	80.0 $\pm$ 33.9	286.0 $\pm$ 81.0	57.4 $\pm$ 20.2	–	–	3.6	1	NG	NG

**Notes.** The columns correspond to: (1) Identifier of the SQ H $\alpha$  emission regions; (2) Integrated [OII] $\lambda$ 3727 flux, relative to H $\beta$ =100, and its uncertainty; (3) Integrated [OIII] $\lambda$ 5007 flux, relative to H $\beta$ =100, and its uncertainty; (4) Integrated H $\alpha$ , relative to H $\beta$ =100, flux and its uncertainty; (5) Integrated [NII] $\lambda$ 6584, relative to H $\beta$ =100, flux and its uncertainty; (6) Integrated [SII] $\lambda$ 6716, relative to H $\beta$ =100, flux and its uncertainty; (7) Integrated [SII] $\lambda$ 6731, relative to H $\beta$ =100, flux and its uncertainty; (8)  $A_v$  extinction (mag); (9) Velocity of the region belongs to the LV (0) or HV (1) sub-sample; (10) Global localisation zone; (11) Local zone. “\*” ID 1 was assigned to the galaxy NGC7320c in the kinematical study done in paper I. “†” Line ratios of the regions where H $\beta$  is not measured; these line ratios are computed by estimating an H $\beta$  flux ( $3\sigma$ , see paper I) value and are not used in our analysis. “ $\nabla$ ” These line ratios may be affected by the kinematics and the conspicuous complex line profile of the region. For regions with two velocity components we use “ $a$ ” and “ $b$ ” for low- and high-velocity components, respectively.

**Table C.2.** Star formation rate,  $H\alpha$  luminosity, BPT classification, and radial velocity sub-sample.

(1) Region ID	(2) SFR ( $\times 10^{-3} M_{\odot} \text{ yr}^{-1}$ )	(3) $L_{H\alpha}$ ( $\times 10^{38} \text{ erg s}^{-1}$ )	(4) BPT	(5) Vel	(1) Region ID	(2) SFR ( $\times 10^{-3} M_{\odot} \text{ yr}^{-1}$ )	(3) $L_{H\alpha}$ ( $\times 10^{38} \text{ erg s}^{-1}$ )	(4) BPT	(5) Vel
2	12.81±0.69	16.21±0.87	SF	1	91	4.29±0.50	5.43±0.64	SF	0
3	11.08±0.78	14.02±0.99	SF	1	92	–	6.18±0.48	AGN	0
4	27.53±0.70	34.84±0.89	SF	1	96	19.53±2.10	24.72±2.66	SF	1
5	–	0.63±0.09	C	1	97	3.88±0.24	4.92±0.31	SF	0
6	17.70±1.35	22.40±1.71	SF	1	98	–	15.75±1.40	C	0
8	31.37±1.80	39.71±2.27	SF	1	102 <sup>a</sup>	3.40±0.63	4.30±0.80	SF	0
9	10.26±0.46	12.99±0.58	SF	1	104 <sup>b</sup>	11.35±1.59	14.36±2.01	SF	1
10	39.85±0.87	50.44±1.10	SF	1	109	0.54±0.13	0.69±0.17	SF	1
11	3.33±0.24	4.21±0.30	SF	1	112	23.20±1.29	29.37±1.63	SF	0
12	1.66±0.16	2.10±0.21	SF	1	113	3.69±0.55	4.68±0.70	SF	1
13	76.48±1.61	96.82±2.03	SF	1	117	119.16±2.67	150.84±3.38	SF	0
14	94.95±4.06	120.19±5.14	SF	1	120	–	20.64±1.11	C	0
15	196.79±5.31	249.10±6.72	SF	1	121	139.98±6.46	177.19±8.18	SF	1
24	29.67±2.38	37.55±3.01	SF	1	122	733.22±13.18	928.12±16.69	SF	1
25	17.79±1.51	22.52±1.91	SF	1	123	0.57±0.08	0.72±0.10	SF	1
26	–	2690.21±192.90	AGN	1	125	7.57±0.98	9.58±1.24	SF	0
27	–	552.11±55.75	AGN	1	127	14.95±0.80	18.93±1.01	SF	0
29	–	3.45±0.53	AGN	1	128	18.60±1.03	23.54±1.30	SF	0
30	–	23.05±3.23	C	1	129	59.93±2.10	75.86±2.65	SF	0
33	2.31±0.27	2.93±0.34	SF	0	130	26.72±1.25	33.82±1.59	SF	0
35	23.79±2.45	30.12±3.10	SF	1	132	38.31±1.36	48.49±1.72	SF	0
39	6.37±0.58	8.06±0.73	SF	0	133	94.48±1.55	119.59±1.97	SF	0
40	–	11.44±1.22	C	1	134	13.96±1.16	17.66±1.46	SF	0
42	13.18±0.81	16.68±1.03	SF	0	136	33.43±1.69	42.32±2.14	SF	0
43	–	3.63±0.48	C	0	137	43.84±2.03	55.50±2.57	SF	0
45	12.63±1.32	15.99±1.67	SF	0	138	32.01±1.18	40.52±1.49	SF	0
46	12.23±1.01	15.48±1.28	SF	0	139	19.86±0.64	25.14±0.81	SF	0
47	0.67±0.10	0.85±0.12	SF	0	140	21.83±1.51	27.63±1.91	SF	0
48	6.19±0.96	7.83±1.22	SF	0	141	42.05±1.28	53.22±1.62	SF	0
50	3.00±0.42	3.79±0.53	SF	0	142	31.38±1.33	39.73±1.68	SF	0
51 <sup>b</sup>	15.59±2.35	19.73±2.97	SF	1	143	29.21±1.43	36.98±1.81	SF	0
52	41.39±1.85	52.39±2.34	SF	0	146	44.23±1.39	55.99±1.76	SF	0
53	–	0.82±0.15	C	0	147	8.64±1.08	10.94±1.37	SF	0
54	–	2.28±0.33	C	0	148	8.24±0.74	10.43±0.94	SF	0
58 <sup>a</sup>	–	7.57±1.26	AGN	0	149	2.93±0.34	3.70±0.43	SF	0
59 <sup>a</sup>	–	10.63±1.54	C	0	150	5.24±0.49	6.63±0.61	SF	0
59 <sup>b</sup>	36.96±7.87	46.78±9.96	SF	1	151	–	2.43±0.22	C	0
60 <sup>a</sup>	–	1.26±0.19	C	0	152	10.59±0.81	13.41±1.02	SF	0
60 <sup>b</sup>	11.77±2.09	14.90±2.64	SF	1	153	25.37±1.31	32.12±1.65	SF	0
64	6.14±0.63	7.77±0.80	SF	1	154	19.76±0.86	25.01±1.09	SF	0
65	36.82±2.38	46.60±3.01	SF	0	155	15.12±0.82	19.14±1.04	SF	0
66 <sup>a</sup>	–	17.69±2.30	AGN	0	156	2.69±0.23	3.40±0.29	SF	0
67	–	8.74±1.23	C	0	157	19.74±1.18	24.98±1.49	SF	0
68 <sup>a</sup>	–	16.09±1.70	C	0	159	14.09±1.04	17.84±1.32	SF	0
69 <sup>a</sup>	–	1.52±0.23	C	0	160	6.16±0.66	7.80±0.84	SF	0
70	14.75±1.00	18.68±1.27	SF	0	164	85.55±1.73	108.29±2.19	SF	0
71	–	2.83±0.32	C	0	165	93.67±2.09	118.57±2.65	SF	0
74	14.51±1.27	18.37±1.61	SF	1	166	53.28±1.53	67.44±1.93	SF	0
75	17.09±1.11	21.63±1.41	SF	0	167	34.23±1.17	43.33±1.48	SF	0
76 <sup>a</sup>	7.37±0.99	9.33±1.26	SF	0	168	8.00±0.30	10.12±0.39	SF	0
76 <sup>b</sup>	3.56±0.67	4.51±0.85	SF	1	169	7.31±0.38	9.26±0.48	SF	0
77	8.81±0.92	11.15±1.16	SF	1	170	5.95±0.32	7.54±0.40	SF	0
78	2.20±0.31	2.78±0.39	SF	0	171	10.65±0.47	13.48±0.60	SF	0
81 <sup>a</sup>	–	2.45±0.39	C	0	172	23.95±0.84	30.32±1.06	SF	0
82	7.07±0.39	8.95±0.50	SF	0	173	21.09±0.73	26.69±0.92	SF	0
83 <sup>b</sup>	22.20±3.06	28.10±3.87	SF	1	174	24.79±0.76	31.38±0.96	SF	0
86 <sup>a</sup>	–	15.92±3.06	AGN	0	176	90.27±9.22	114.26±11.66	SF	1
90	–	19.96±1.45	C	0					

**Notes.** The columns correspond to: (1) Identifier of the HII region; (2) Star formation rate ( $\times 10^{-3} M_{\odot} \text{ yr}^{-1}$ ); (3)  $H\alpha$  luminosity ( $\times 10^{38} \text{ erg s}^{-1}$ ); (4) BPT classification; (5) Velocity of the region belongs to the LV (0) or the HV (1) sub-samples. For regions with two velocity components we use ‘<sup>a</sup>’ and ‘<sup>b</sup>’ for low- and high-velocity components, respectively.

**Table C.3.** Oxygen abundances for the SQ HII regions using N2 and O3N2 (Pérez-Montero & Contini 2009), and R calibrators (Pilyugin & Grebel 2016), respectively, nitrogen to oxygen abundances ratio using Pilyugin & Grebel (2016), and radial velocity sub-sample.

(1)	(2)	(3)	(4)	(5)	(6)	(1)	(2)	(3)	(4)	(5)	(6)
Region ID	$12+\log(\text{O}/\text{H})_{\text{N2}}$	$12+\log(\text{O}/\text{H})_{\text{O3N2}}$	$12+\log(\text{O}/\text{H})_{\text{R}}$	$\log(\text{N}/\text{O})_{\text{PI16}}$	Vel	Region ID	$12+\log(\text{O}/\text{H})_{\text{N2}}$	$12+\log(\text{O}/\text{H})_{\text{O3N2}}$	$12+\log(\text{O}/\text{H})_{\text{R}}$	$\log(\text{N}/\text{O})_{\text{PI16}}$	Vel
2	8.30±0.11	8.35±0.05	8.22±0.11	-1.29±0.13	1	113	8.72±0.11	8.60±0.07	–	–	1
3	8.61±0.09	8.48±0.06	8.46±0.10	-1.17±0.14	1	117	8.57±0.02	8.49±0.02	8.54±0.02	-0.83±0.05	0
4	8.55±0.03	8.47±0.02	8.49±0.04	-0.98±0.09	1	121	8.63±0.04	8.48±0.03	8.51±0.05	-1.05±0.09	1
6	8.48±0.10	8.36±0.06	–	–	1	122	8.46±0.02	8.41±0.02	8.45±0.03	-0.99±0.06	1
8	8.59±0.07	8.59±0.05	–	–	1	123	8.79±0.11	8.60±0.06	–	–	1
9	8.61±0.04	8.50±0.03	8.55±0.04	-0.86±0.09	1	125	8.74±0.09	8.65±0.07	8.58±0.09	-0.95±0.14	0
10	8.46±0.03	8.38±0.02	8.47±0.03	-0.95±0.06	1	127	8.77±0.04	8.64±0.03	8.66±0.02	-0.65±0.08	0
11	8.66±0.06	8.54±0.04	8.60±0.04	-0.74±0.11	1	128	8.75±0.04	8.59±0.05	8.60±0.04	-0.97±0.12	0
12	8.62±0.09	8.63±0.06	–	–	1	129	8.71±0.03	8.60±0.03	8.59±0.03	-0.88±0.07	0
13	8.55±0.02	8.42±0.02	8.54±0.03	-0.84±0.09	1	130	8.65±0.04	8.64±0.05	8.60±0.03	-0.63±0.10	0
14	8.72±0.03	8.66±0.03	8.60±0.03	-0.79±0.10	1	132	8.72±0.03	8.57±0.02	8.61±0.02	-0.86±0.07	0
15	8.59±0.03	8.49±0.02	8.58±0.02	-0.74±0.07	1	133	8.67±0.01	8.51±0.01	8.61±0.01	-0.77±0.04	0
24	8.76±0.05	8.70±0.05	8.65±0.04	-0.67±0.10	1	134	8.75±0.06	8.70±0.06	8.61±0.05	-0.79±0.12	0
25	8.81±0.05	8.74±0.05	–	–	1	136	8.74±0.04	8.58±0.03	8.62±0.04	-0.87±0.10	0
33	8.70±0.09	8.59±0.05	8.62±0.06	-0.74±0.11	0	137	8.76±0.03	8.64±0.03	8.65±0.03	-0.74±0.09	0
35	8.84±0.08	8.70±0.05	8.62±0.08	-1.01±0.10	1	138	8.75±0.03	8.63±0.03	8.63±0.02	-0.77±0.08	0
39	8.60±0.09	8.47±0.04	8.55±0.07	-0.87±0.11	0	139	8.63±0.03	8.54±0.02	8.61±0.02	-0.64±0.07	0
42	8.64±0.07	8.56±0.04	8.53±0.06	-0.95±0.10	0	140	8.74±0.05	8.62±0.04	8.62±0.04	-0.82±0.10	0
45	8.79±0.08	8.64±0.06	8.61±0.08	-1.00±0.12	0	141	8.69±0.02	8.57±0.02	8.60±0.02	-0.81±0.06	0
46	8.58±0.08	8.62±0.06	–	–	0	142	8.77±0.03	8.61±0.03	8.66±0.02	-0.74±0.08	0
47	8.81±0.09	8.72±0.06	8.68±0.05	-0.58±0.13	0	143	8.77±0.03	8.65±0.03	8.66±0.02	-0.69±0.09	0
48	8.82±0.11	8.65±0.07	8.66±0.09	-0.85±0.15	0	146	8.75±0.02	8.64±0.03	8.64±0.02	-0.72±0.08	0
50	8.83±0.09	8.66±0.06	8.62±0.10	-1.06±0.12	0	147	8.73±0.09	8.57±0.06	8.49±0.12	-1.25±0.15	0
51 <sup>b</sup>	8.71±0.12	8.63±0.07	8.50±0.13	-1.11±0.13	1	148	8.75±0.06	8.67±0.06	8.60±0.06	-0.88±0.13	0
52	8.71±0.04	8.66±0.04	8.59±0.04	-0.82±0.09	0	149	8.73±0.09	8.62±0.06	8.58±0.08	-0.93±0.14	0
59 <sup>b</sup>	8.39±0.13	8.52±0.07	7.98±0.17	-1.58±0.13	1	150	8.69±0.07	8.65±0.06	8.56±0.07	-0.90±0.11	0
60 <sup>b</sup>	8.71±0.09	8.55±0.06	8.44±0.12	-1.32±0.13	1	152	8.56±0.08	8.57±0.06	8.51±0.07	-0.88±0.12	0
64	8.72±0.12	8.74±0.07	8.60±0.08	-0.75±0.11	1	153	8.66±0.04	8.60±0.04	8.57±0.04	-0.84±0.09	0
65	8.65±0.06	8.60±0.06	8.50±0.07	-1.01±0.14	0	154	8.70±0.03	8.58±0.03	8.63±0.02	-0.70±0.09	0
70	8.79±0.05	8.71±0.05	8.61±0.05	-0.92±0.10	0	155	8.59±0.05	8.45±0.04	8.54±0.04	-0.89±0.10	0
74	8.57±0.11	8.69±0.06	8.42±0.10	-1.02±0.11	1	156	8.63±0.08	8.54±0.04	8.56±0.06	-0.86±0.10	0
75	8.69±0.09	8.65±0.05	8.60±0.06	-0.75±0.11	0	157	8.67±0.05	8.55±0.04	8.59±0.04	-0.83±0.10	0
76 <sup>a</sup>	8.77±0.09	8.70±0.05	8.58±0.09	-0.97±0.10	0	159	8.73±0.05	8.64±0.05	–	–	0
76 <sup>b</sup>	8.76±0.12	8.67±0.07	8.56±0.12	-1.01±0.13	1	160	8.66±0.09	8.50±0.06	–	–	0
77	8.66±0.11	8.64±0.06	8.56±0.09	-0.85±0.13	1	164	8.63±0.02	8.50±0.02	8.57±0.02	-0.85±0.05	0
78	8.42±0.12	8.52±0.06	8.27±0.13	-1.23±0.14	0	165	8.62±0.02	8.50±0.02	8.57±0.02	-0.83±0.05	0
82	8.52±0.07	8.46±0.03	8.46±0.06	-1.01±0.09	0	166	8.62±0.03	8.47±0.02	8.56±0.02	-0.88±0.06	0
83 <sup>b</sup>	8.52±0.10	8.55±0.05	8.36±0.10	-1.16±0.11	1	167	8.52±0.04	8.43±0.03	8.47±0.04	-1.00±0.07	0
91	8.71±0.09	8.66±0.06	8.55±0.08	-0.95±0.12	0	168	8.57±0.04	8.45±0.03	8.55±0.03	-0.83±0.08	0
96	8.60±0.09	8.62±0.06	8.44±0.09	-1.05±0.12	1	169	8.63±0.05	8.50±0.03	8.56±0.04	-0.90±0.07	0
97	8.35±0.12	8.28±0.05	8.45±0.07	-0.92±0.12	0	170	8.55±0.06	8.47±0.03	8.56±0.03	-0.70±0.09	0
102 <sup>a</sup>	8.77±0.11	8.61±0.06	8.60±0.12	-1.01±0.15	0	171	8.57±0.05	8.44±0.02	8.54±0.04	-0.86±0.08	0
104 <sup>b</sup>	8.67±0.09	8.67±0.06	8.49±0.09	-1.02±0.11	1	172	8.37±0.06	8.30±0.03	8.46±0.04	-0.91±0.07	0
109	8.75±0.14	8.66±0.07	–	–	1	173	8.49±0.04	8.39±0.03	8.45±0.04	-1.04±0.08	0
112	8.72±0.04	8.56±0.03	8.62±0.03	-0.85±0.08	0	174	8.59±0.04	8.47±0.03	8.49±0.04	-1.06±0.08	0
						176	8.52±0.12	8.55±0.07	8.27±0.15	-1.31±0.16	1

**Notes.** The columns correspond to: (1) Identifier of the HII region; (2) Oxygen abundances using N2 calibrator (Pérez-Montero & Contini 2009); (3) Oxygen abundances using O3N2 calibrator (Pérez-Montero & Contini 2009); (4) Oxygen abundances using R calibrator (Pilyugin & Grebel 2016); (5) Nitrogen to oxygen abundances ratio using Pilyugin & Grebel (2016) calibrator; (6) Velocity of the region belongs to the LV (0) or the HV (1) sub-samples. For regions with two velocity components we use ‘<sup>a</sup>’ and ‘<sup>b</sup>’ for low- and high-velocity components, respectively.